Relative Contributions of Sea Surface Temperature and Atmospheric Nonlinearities to ENSO Asymmetrical Rainfall Response

G. SRINIVAS,[a] J. VIALARD,[a] M. LENGAIGNE,[b] T. IZUMO,[c] AND E. GUILYARDI[a,d]

[a] *LOCEAN-IPSL, Sorbonne Université (UPMC, Univ Paris 06) CNRS-IRD-MNHN, Paris, France*
[b] *MARBEC, University of Montpellier, CNRS, IFREMER, IRD Sète, France*
[c] *EIO, Ifremer, ILM, UPF, IRD, Ifremer Tahiti, France*
[d] *NCAS-Climate, University of Reading, Reading, United Kingdom*

ABSTRACT: Here, we investigate the relative roles of atmospheric nonlinearities and asymmetrical sea surface temperature (SST) forcing in the El Niño–Southern Oscillation (ENSO) asymmetrical rainfall response. Applying a vertically integrated water vapor budget to the ERA5 reanalysis leads to a simple analytical equation for precipitation anomalies. This formulation reveals that ENSO rainfall anomalies are dominated by the linear component of the dynamical term (i.e., the anomalous moisture convergence due to the effect of circulation anomalies on climatological humidity). Nonlinearities in this term and the linear thermodynamical term (i.e., the effect of climatological circulation on humidity anomalies) both strengthen central Pacific rainfall anomalies for both ENSO phases. In contrast, the nonlinear term associated with the effect of anomalous divergence on anomalous moisture (i.e., the mixed term) weakens La Niña dry and strengthens El Niño wet anomalies, in particular during extreme El Niño events when it contributes to about 40% of the eastern Pacific wet anomalies. Overall, atmospheric nonlinearities directly account for ~70% of the positively skewed ENSO rainfall distribution east of the date line, and ~50% of the negatively skewed rainfall distribution in the western Pacific. The remaining ENSO rainfall asymmetries are attributable to the asymmetrical ENSO SST pattern. This asymmetrical SST pattern also has contributions from atmospheric nonlinearities through the Bjerknes feedback loop, in addition to those from oceanic nonlinearities. Our estimates are thus likely a lower bound of the contribution of atmospheric nonlinearities to the overall ENSO rainfall asymmetry.

KEYWORDS: Tropics; Rainfall; Budgets; Atmosphere-ocean interaction; ENSO; Idealized models

---

1. Introduction

El Niño–Southern Oscillation (ENSO) arises from air–sea interactions in the tropical Pacific (e.g., Timmermann et al. 2018) and affects climate worldwide through atmospheric teleconnections (Taschetto et al. 2020). ENSO dominates Earth's year-to-year climate variations, impacting ecosystems and societies globally (Holbrook et al. 2020; Lehodey et al. 2020). The warm phase of ENSO is characterized by anomalously warm sea surface temperature (SST) anomalies in the central and eastern equatorial Pacific and by enhanced deep atmospheric convection and westerly wind anomalies in the central equatorial Pacific. While La Niña (i.e., the cold ENSO phase) can broadly be viewed as a mirror image of El Niño, asymmetries between these two ENSO phases have recently become a prominent research interest (e.g., An et al. 2020). This interest relates to the fact that El Niño events can occasionally reach much larger amplitudes than La Niña events, like in 1982, 1997, and 2015. There is a complete reorganization of deep atmospheric convection during these extreme El Niño events, including an equatorial shift of the intertropical convergence zone that leads to large rainfall anomalies in the otherwise dry eastern equatorial Pacific (e.g., Takahashi et al. 2011; Cai et al. 2014; Santoso et al. 2017). This has motivated in-depth studies on the drivers of these extreme El Niño events (see Santoso et al. 2017), and more generally on asymmetries between El Niño and La Niña (An et al. 2020).

As mentioned above, the most obvious ENSO asymmetry is related to its amplitude, with stronger El Niño than La Niña SST and rainfall anomalies in the eastern Pacific (e.g., Deser and Wallace 1987; Burgers and Stephenson 1999; An and Jin 2004). This amplitude asymmetry is also associated with various pattern asymmetries. La Niña SST and rainfall anomalies are shifted westward and have a wider latitudinal extension relative to El Niño anomalies (Hoerling et al. 1997; Kang and Kug 2002; Takahashi et al. 2011; Dommenget et al. 2013). Also, El Niño patterns tend to be more diverse than La Niña patterns, with smaller amplitude El Niño events being confined in the central Pacific, while strong events extend up to the South American coast (e.g., Kug et al. 2009; Takahashi et al. 2011; Capotondi et al. 2020). On the other hand, strong La Niña events tend to be shifted west relative to weak La Niña events (Dommenget et al. 2013). There is also a marked asymmetry in ENSO phase changes: El Niño events tend to decay rapidly after their peak and transition to La Niña events, while La Niña events can persist a second year and are rarely followed by an El Niño event (e.g., Larkin and Harrison 2002; Ohba and Ueda 2009; Okumura and Deser 2010; Choi et al. 2013). This may indicate that some phases of ENSO are more predictable than some others (e.g., Larson and Kirtman 2017; Planton et al. 2018, 2022) and hence have practical applications for seasonal forecasts.

Nonlinearities are required to explain ENSO asymmetries (An et al. 2020). Oceanic nonlinearities have been proposed to contribute to these asymmetries (e.g., nonlinear dynamical

heating, tropical instability waves; see An et al. 2020). We will come back to the role of oceanic nonlinearities in the discussion section, but here we focus on atmospheric nonlinearities, which some studies argue to be the primary source of ENSO overall asymmetry (Geng et al. 2019) including its pattern asymmetry (Geng et al. 2020). Subseasonal synoptic wind events named "westerly wind events" (WWEs) play a vital role in ENSO development (e.g., Lengaigne et al. 2005). While those events are partly random, they become more probable and expand eastward during El Niño (e.g., Lengaigne et al. 2004; Eisenman et al. 2005; Puy et al. 2016). This "multiplicative noise forcing" associated with WWEs acts to increase El Niño amplitude and decrease the predictability of El Niño events relative to La Niña events (e.g., Jin et al. 2007; Levine and Jin 2010; Planton et al. 2022) and strongly contributes to the genesis of strong El Niño events (e.g., Puy et al. 2017). The low-frequency wind stress (e.g., Hoerling et al. 1997; Kang and Kug 2002) and heat flux (e.g., Lloyd et al. 2012; Bellenger et al. 2014) response to a unit SST anomaly also tends to be larger during El Niño than during La Niña events. This wind stress asymmetry also favors larger El Niño events (Kang and Kug 2002; Frauen and Dommenget 2010; Choi et al. 2013) while the heat flux asymmetry limits this amplitude asymmetry (Im et al. 2015). All these nonlinear atmospheric processes are related to the development of deep atmospheric convection, driving surface wind anomalies through Matsuno–Gill dynamics and influencing surface heat fluxes via their joint effect on shortwave and latent heat fluxes.

Deep atmospheric convection and the associated rainfall indeed play a critical role in the nonlinearity of the tropical atmosphere. While the low-level equatorial atmospheric circulation response to diabatic heating is generally considered quite linear (DeWeaver and Nigam 2002), there is a strong nonlinear dependence of the atmospheric deep convection on SSTs, with convection preferentially developing above a ~27°C threshold (e.g., Gadgil et al. 1984; Graham and Barnett 1987). Previous studies have proposed that this nonlinearity plays a significant role in the westward shift of La Niña rainfall and wind anomalous patterns relative to those of El Niño (Hoerling et al. 1997; Kang and Kug 2002; Ham and Kug 2012). Background SST exceeds the convective threshold west of the date line, and warm anomalies raise SST above the convective threshold mainly east of the date line, while cold anomalies inhibit convection west of the date line, hence leading to the westward shift of convective and wind anomalies during La Niña compared to El Niño. Through a series of idealized experiments with an atmospheric general circulation model (AGCM) forced by opposite anomalous SST patterns, Hoerling et al. (2001) demonstrated that atmospheric nonlinearities mostly matter for strong El Niño events, while the atmospheric response is predominantly linear for weaker ENSO SST forcing. Forced and coupled model experiments (Kang and Kug 2002) and a stability analysis applied to observationally derived products (Im et al. 2015) both indicate that the nonlinearity of atmospheric convection plays a significant role in ENSO asymmetry, through its control of the eastward shift of El Niño wind anomalies. The nonlinearity of the

convective/rainfall response to SST also plays a key role in the development of the strong east Pacific El Niño events (e.g., Takahashi and Dewitte 2016).

The above studies point out the key role of the nonlinear rainfall response to SST for ENSO asymmetries. However, only a few studies did attempt to identify the physical processes behind this nonlinear rainfall response to SST from the perspective of the water budget. Chung et al. (2014) and Chung and Power (2014) did apply a vertically integrated water budget analysis to idealized AGCM experiments forced by El Niño and La Niña patterns of varying amplitudes. Terms of this vertically integrated water budget include the influence of 1) circulation anomalies on the background humidity (referred below as the dynamical term), 2) background circulation on humidity anomalies (referred below as the thermodynamical term), and 3) anomalous circulation on humidity anomalies (referred below as the mixed term). They found that the dynamical term in general dominates ENSO-induced moisture convergence, and its nonlinearity is responsible for the eastward shift of El Niño rainfall pattern relative to that of La Niña, with the nonlinear mixed term having a smaller contribution. Using a similar modeling framework, Chung and Power (2015) however demonstrated that, in addition to these atmospheric nonlinearities, differences between the canonical and strong El Niño SST patterns also contribute to the asymmetrical ENSO rainfall response through changes in the dynamical term of the vertically integrated water budget.

These studies, based on atmospheric experiments with a single AGCM, suggest that both atmospheric nonlinearities related to the dynamical term and SST asymmetries contribute to the ENSO asymmetrical rainfall response, but do not quantify their relative importance. In the present study, we diagnose the contribution of atmospheric nonlinearities and SST asymmetries to the ENSO asymmetrical precipitation response in detail using a dataset more constrained by observations, namely the latest European Centre of Medium-Range Forecast (ECMWF) reanalysis (ERA5; Hersbach et al. 2020). We use a vertically integrated water budget approach to derive an equation for precipitation anomalies as a function of SST and surface layer divergence anomalies and their background seasonal cycle. This equation is used to separate precipitation anomalies into parts that linearly and nonlinearly depend on SST anomalies. This allows diagnosing the relative contribution of atmospheric nonlinearities and SST asymmetries to the ENSO asymmetrical precipitation response, as well as identifying the associated physical processes.

The rest of the paper is organized as follows. Section 2 describes the methods and datasets. In section 3, we apply the vertically integrated water budget to the climatological and ENSO rainfall anomalies and discuss the dominant balance. Based on these results, we derive a simple equation for precipitation anomalies in section 4. In section 5, we use that equation to discuss the physical processes that contribute to the asymmetrical ENSO rainfall response, as well as the relative contribution of atmospheric nonlinearities and asymmetrical SST forcing to this asymmetry. Finally, section 6 provides a summary and discusses our results.

2. Datasets and methods

We use the latest version of European Centre for Medium-Range Weather Forecasts (ECMWF) reanalysis (ERA5; Hersbach et al. 2020) produced using 4D-Var data assimilation and improved physical parameterizations (in particular convection and microphysics). This dataset has a $0.5° \times 0.5°$ horizontal resolution and 137 hybrid sigma/pressure levels, with the top level at 0.01 hPa. To investigate how SST modulates the atmospheric water vapor budget, we use the following monthly mean fields: SST, precipitation, evaporation (two-dimensional fields at the surface level), specific humidity, and zonal and meridional wind components (three-dimensional fields on pressure levels). The three-dimensional horizontal divergence used in our budgets is recomputed from the zonal and meridional wind components. ERA5 also provides monthly averages of the vertically integrated horizontal moisture convergence, which we used in combination with the other monthly data to distinguish the low-frequency and high-frequency scale variations contributions to the water vapor budget calculation.

In addition, we use the following ancillary datasets for evaluation purposes: monthly mean Global Precipitation Climatology Project (GPCP) (version 2.3; Adler et al. 2018) rainfall (1979–2019), 10-m wind retrieved from the SeaWinds instrument aboard the National Aeronautics and Space Administration (NOAA) QuikSCAT satellite (1999–2009; Hoffman and Leidner 2005), and surface-level relative humidity from the Atmospheric Infrared Sounder (AIRS; Olsen et al. 2017) satellite product (2005–19). In the following sections, the monthly climatological seasonal cycle is computed over the 1979–2019 period except for Fig. 1, where the ERA5 climatology is computed over the longest period available for each observational dataset. Since we focus on seasonal and longer time scales typical of ENSO, a 3-month Hanning filter is systematically applied to all monthly mean fields.

Since our results are based on the ERA5 dataset, let us briefly evaluate this product. Nogueira (2020) showed that this product is improved over ERA-Interim (herein ERA-I; Dee et al. 2011) in the tropics, both in terms of bias, correlation, and root-mean square error. Nogueira's (2020) process-based analysis points to an improved representation of the moisture sinks and sources in the tropics, an important feature for our budget analysis. He however also diagnosed an overestimated moisture-flux convergence in the tropics, leading to excessive precipitation in ERA5. Figure 1 complements this analysis by providing a qualitative evaluation of ERA5 climatological rainfall, surface circulation, and relative humidity in the tropics against observationally derived estimates. Figures 1a and 1b indicate that ERA5 reproduces reasonably well the main tropical rainfall bands such as the intertropical convergence zone (ITCZ) and South Pacific convergence zone (SPCZ), but tends to overestimate rainfall amount in those areas (by ~30% on average for regions where GPCP climatological rainfall estimate is >6 mm day^{-1}; see Fig. 1c). ERA5 reproduces the surface circulation structure well (Figs. 1a,b) but underestimates the surface wind convergence in rainy areas (Fig. 2c). This suggests that the rainfall overestimation
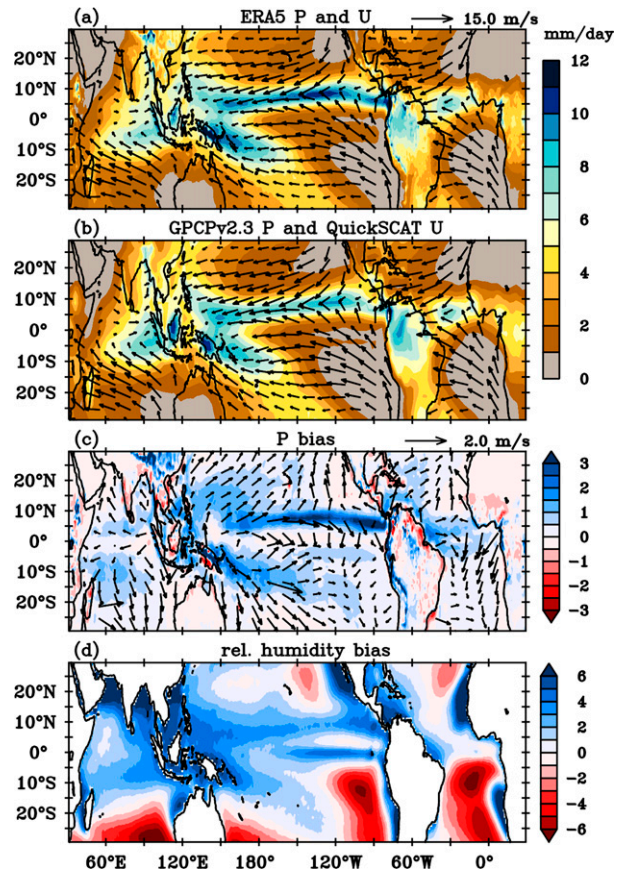

FIG. 1. Climatological precipitation (shading; mm day^{-1}) and 10-m winds (vectors; m s^{-1}) for (a) ERA5 and (b) observations. Bias (i.e., ERA5 minus observed) of (c) precipitation (shading; mm day^{-1}) and 10-m wind (vectors; m s^{-1}), and (d) relative humidity (shading; %). Observations used are GPCPv2.3 for precipitation, QuikSCAT for winds, and AIRS for relative humidity. For consistency, ERA5 climatology is computed for the period over which each observational dataset is available (1979–2019 for GPCPv2.3, 1999–2009 for QuikSCAT, and 2005–19 for AIRS).

is not attributable to circulation biases, but rather to biases in the lower tropospheric water vapor content. Comparison of ERA5 surface relative humidity with that from AIRS confirms this hypothesis, pointing to a wet bias of up to 6% over most of the three tropical basins (Fig. 1d). The overestimated ERA5 rainfall in rainy regions is thus likely linked to thermodynamical rather than dynamical biases, as also suggested by the analyses of Nogueira (2020). In the discussion section, we will come back to the potential consequences of these biases on our results. We do not show ENSO rainfall anomalies from ERA5 here, but will show later that they agree quite closely with those from GPCP (Figs. 3 and 4).

We also compute El Niño and La Niña composites using NOAA's operational definition for ENSO events (Trenberth et al. 2020), based on the oceanic Niño index (ONI). This index corresponds to a 3-month running mean of SST anomalies in the Niño-3.4 region (5°N–5°S, 120°–170°W). Following the NOAA methodology, we define an El Niño (La Niña)
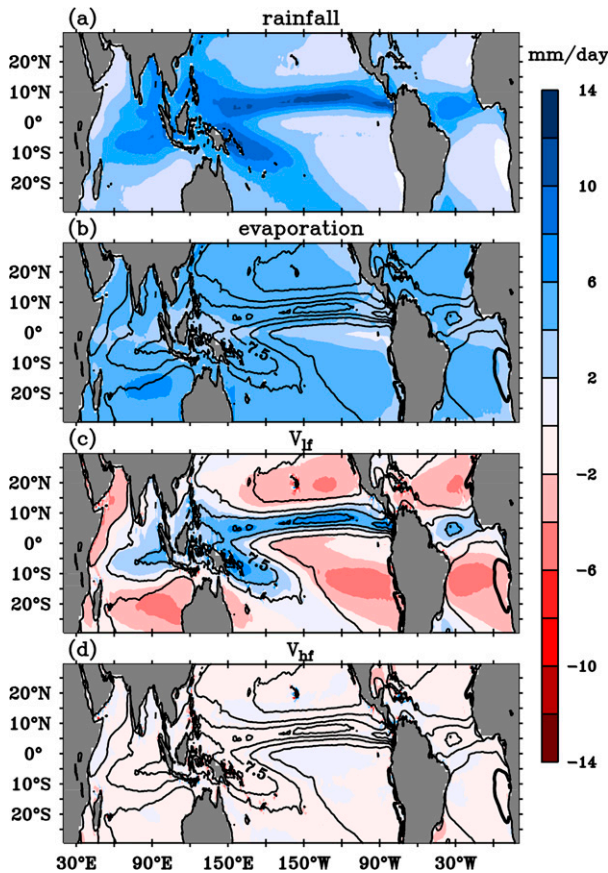
FIG. 2. Climatology of vertically integrated moisture budget terms (mm day^{-1}): (a) precipitation, (b) evaporation, and (c) low-frequency (V_{lf}) and (d) high-frequency (V_{hf}) components of the vertically integrated moisture convergence (VIMC). Climatological precipitation from (a) are overlaid as contours in (b)–(d). Here and in the rest of the manuscript, the climatology is computed over 1979–2019. See Eq. (1) for ERA5 vertically integrated moisture budget: rainfall [in (a)] is equal to the sum of (b)–(d) plus negligible terms (see text for details). Seasonal V anomalies have been broken down into contributions from low (~90 day and longer; see text for details) and high frequencies (less than ~90 days).

event when this ONI exceeds (falls below) 0.5°C (−0.5°C) during more than 5 consecutive months. We further consider that an El Niño is an "extreme" El Niño when the ONI index exceeds 2°C, while other El Niño events are defined as moderate. Based on the above criteria, 1982/83, 1997/98, and 2015/16 fall in the extreme El Niño events category; 1979/80, 1986/87, 1987/88, 1991/92, 1994/95, 2002/03, 2004/05, 2006/07, 2009/10, 2014/15, and 2018/19 are classified as moderate El Niño events; and 1980/81, 1983/84, 1984/85, 1985/86, 1988/89, 1995/96, 1996/97, 1998/99, 1999/2000, 2000/01, 2005/06, 2007/08, 2008/09, 2010/11, 2011/12, 2016/17, and 2017/18 are classified as La Niña events. Because we use the ERA5 data product and we do not detrend SST, two cold events (1980/81 and 1996/97) and one warm event (1979/80) that are slightly below the threshold in NOAA's classification become La Niña or El Niño events in our classification. We did verify that including

or excluding these events when computing composites hardly changes our results. When specifically wanting to highlight general El Niño versus La Niña asymmetries, we merge extreme and moderate El Niño events into a single category (e.g., Figs. 10 and 12). In Fig. 3, where we first present the broad balance that explains both El Niño and La Niña rainfall anomalies, we will simply perform an ENSO composite by combining all three categories (applying a −1 weighting to La Niña years).

3. The vertically integrated water budget

We use a vertically integrated water vapor budget to investigate the main processes that contribute to tropical rainfall. We apply this budget to the total ERA5 precipitation, before investigating anomalies with respect to the climatological seasonal cycle to understand the dominant balance that drive ENSO precipitation anomalies. The vertically integrated atmospheric water vapor budget equation for low-frequency variations (the ⟨ ⟩ operator indicates a 3-month Hanning filter applied to monthly mean values as described in section 2) can be written as follows:

$$\frac{d\langle W\rangle}{dt} = \langle E\rangle - \langle P\rangle + \langle V_{\text{tot}}\rangle + \langle I\rangle. \tag{1}$$

Equation (1) states that low-frequency filtered total atmospheric column water vapor ($\langle W\rangle$) has a source term associated with surface evaporation ($\langle E\rangle$), a sink term associated with precipitation ($\langle P\rangle$), and a sink or source associated with vertically integrated moisture convergence ($\langle V_{\text{tot}}\rangle$) correspond to a residual associated with extra source and sink terms. Some of these extra terms are physical (e.g., changes in cloud liquid and ice water content) while others result from the assimilation increments that constrain ERA5 water content to remain close to the observed values. The storage $d\langle W\rangle/dt$ and residual terms are at least one order of magnitude smaller than other terms in Eq. (1), for climatology as well as for interannual anomalies, and are thus neglected in the remaining of the paper.

In Eq. (2),

$$\langle V_{\text{tot}}\rangle \equiv -\left\langle \nabla\left(\frac{1}{g}\int_{p_s}^{p_t} \mathbf{v}q\,dp\right)\right\rangle = -\nabla\left\langle\frac{1}{g}\int_{p_s}^{p_t} \langle\mathbf{v}\rangle\langle q\rangle + \langle v''q''\rangle dp\right\rangle$$
$$\approx V_{\text{lf}} + V_{\text{hf}}, \tag{2}$$

$\langle V_{\text{tot}}\rangle$ is estimated from the pressure integral between $p_s = 1000$ and $p_t = 300$ hPa, q is the specific humidity, $\mathbf{v}$ is the horizontal wind vector, and g is the gravitational acceleration. Since we are mostly interested in ENSO, which is a low-frequency signal, we further decompose V_{tot} into contributions from intraseasonal (V_{hf}) and low-frequency (V_{lf}) q and $\mathbf{v}$ components. The double prime ($''$) indicates deviations from filtered values ⟨ ⟩. ERA5 provides monthly average values for the vertically integrated moisture convergence V_{tot}: we thus compute V_{lf} from the filtered velocity $\mathbf{v}$ and specific humidity q and obtain V_{hf} as a residual. In the rest of the paper, we drop the ⟨ ⟩ operator and all variables correspond to the monthly mean to which the Hanning filter has been applied.
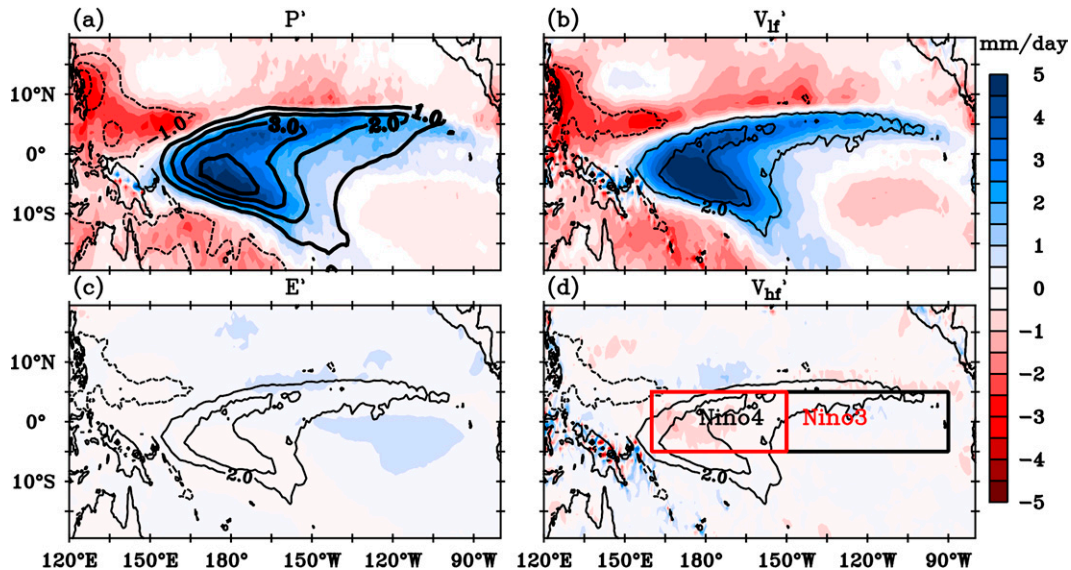
FIG. 3. Composite map of the boreal winter [i.e., December–February (DJF)] ENSO symmetrical anomalous vertically integrated moisture budget terms (mm day^{-1}): (a) precipitation, (b) low-frequency components of the vertically integrated moisture convergence V_{lf}, (c) evaporation, and (d) high-frequency components of the vertically integrated moisture convergence V_{hf}. Observed precipitation anomalies are overlaid as thick contours in (a) and ERA5 precipitation anomalies from (a) are overlaid as thin contours in (b)–(d). The ENSO symmetrical composite is obtained as $1/2 \times$ (El Niño composite − La Niña composite). See section 2 for the years retained as El Niño and La Niña events.

Figure 2 displays the long-term mean of the Eq. (1) dominant terms. The subseasonal component of the vertically integrated moisture convergence V_{hf} marginally contributes to tropical large-scale precipitation (Fig. 2d) and can thus be neglected. As a result, the climatological rainfall (Fig. 2a) results from a balance between evaporation (Fig. 2b) and vertically integrated moisture convergence associated with low-frequency winds and humidity V_{lf} (Fig. 2c). The rainfall spatial structure is mainly controlled by V_{lf} (Fig. 2c) because E is spatially homogeneous (Fig. 2b). Similarly, the rainfall seasonal variations are determined by the V_{lf} variations, with evaporation remaining almost constant throughout the climatological seasonal cycle (not shown).

Let us now discuss the main rainfall balance associated with ENSO. To do so, Figs. 3 and 4 respectively provide an ENSO symmetric component composite and the averaged Niño-3 and Niño-4 (see box boundaries in Fig. 3d) time series of the dominant terms from Eq. (1) interannual anomalies [where a prime ($'$) denotes anomalies with respect to the climatological seasonal cycle]:

$$P' = E' + V'_{hf} + V'_{lf}. \tag{3}$$

The composite of symmetrical ENSO rainfall anomalies from ERA5 match those from GPCP (colors and contours in Fig. 3a) well, with wet anomalies between 10°S and 5°N in the western and central Pacific corresponding to an equatorward shift of the ITCZ and SPCZ, and dry anomalies under the ITCZ and SPCZ poleward portions. The V_{hf} and evaporation interannual anomalies only marginally contribute to symmetric ENSO rainfall anomalies (Figs. 3c,d), which are almost entirely

controlled by the interannual anomalies of the low-frequency vertically integrated moisture convergence: $P' \approx \sim V'_{lf}$. Time series of the water budget interannual anomalies (Fig. 4) further support this balance, with a 0.93 (0.95) correlation and 0.5 (0.73) mm day^{-1} rms error over Niño-3 (Niño-4). It also indicates that this balance holds both for El Niño and La Niña events. This figure also shows that ERA5 interannual anomalies closely follow those from GPCP, both during El Niño and La Niña events, confirming that ERA5 can confidently be used to study ENSO rainfall asymmetry.

This section demonstrated that the low-frequency vertically integrated moisture convergence plays a key role in the large-scale rainfall distribution, as hypothesized by Neelin and Held (1987). It controls the climatological rainfall spatial pattern and seasonal cycle, with an offset associated with the almost constant evaporation rate. ENSO-related interannual rainfall anomalies are controlled by the low-frequency vertically integrated moisture convergence, with evaporation interannual anomalies playing a negligible role. This matches the results from previous moisture budget analyses in the tropical regions (e.g., Rao et al. 1998). Hence, the tropical precipitation anomalies can be approximated as low-frequency vertically integrated moisture convergence anomalies.

4. Precipitation as a function of surface properties

We follow ideas similar to Neelin and Held (1987) and Yu and Neelin (1997) to relate the tropical precipitation to SST. These authors developed an analytical framework that indicates that the vertically integrated moisture convergence due to low frequencies should be proportional to near-surface
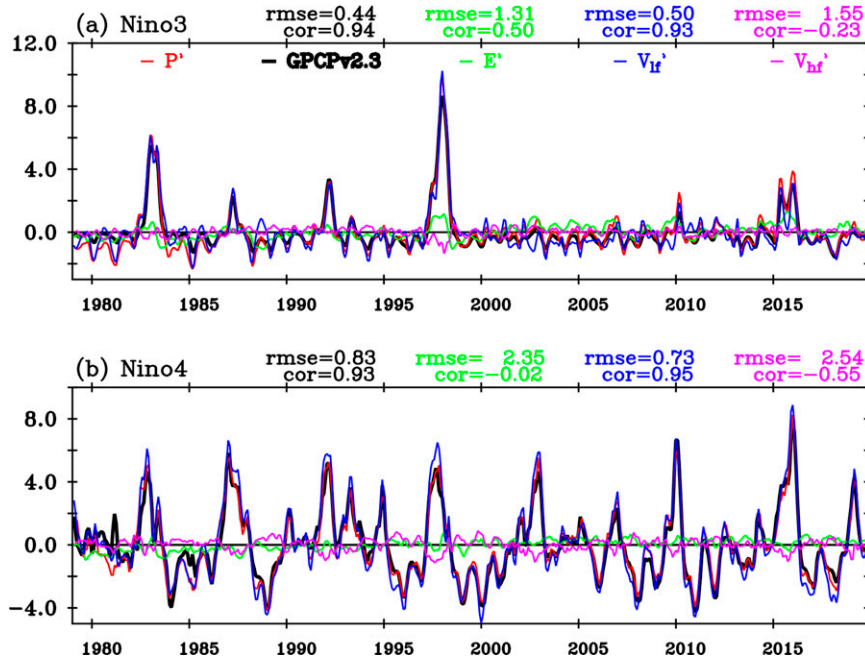
FIG. 4. Time series of interannual anomalies of the ERA5 vertically integrated moisture budget terms (mm day^{-1}): precipitation (red), evaporation (green), low-frequency components of the vertically integrated moisture convergence V_{lf} (blue), and high-frequency components of the vertically integrated moisture convergence V_{hf} (magenta) averaged over (a) Niño-3 and (b) Niño-4 regions. Observed precipitation anomalies are plotted as solid black line. The correlation and root-mean-square error of each curve relative to the ERA-5 interannual rainfall anomalies are indicated above each panel.

divergence [Eq. (4.1) in Yu and Neelin (1997)], with a "gross moisture stratification" proportionality coefficient, which strongly depends on SST (Yu et al. 1998). Some authors have pointed out the use of a single vertical profile is not appropriate to describe the atmospheric divergence and humidity variability in regions such as the ITCZ (e.g., Back and Bretherton 2006), where changes in vertical profiles respond locally not only to SST but also to large-scale reconfigurations of the atmospheric circulation (e.g., Huaman and Schumacher 2018). As we will show later, this approach allows us to derive a rainfall equation that performs very well in the Niño-3 and Niño-4 regions, which are most relevant for discussing ENSO variability. Readers can refer to appendix A for a simplified derivation of such a relation, but we briefly summarize the salient steps here. Vertically integrated humidity advection is generally weak in the tropics (not shown). Figure 5 shows climatological profiles of moisture, divergence, and moisture divergence in Niño-3 and Niño-4, as well as the typical vertical structure of ENSO-related signals (obtained through regression on normalized Niño-3.4 SST anomalies). Because of the colder temperature at upper levels and the Clausius–Clapeyron relationship, specific humidity decays roughly exponentially with height (Fig. 5a). As a result, most of the moisture convergence/divergence largely occurs within the 1000–850-hPa layer (Fig. 5c). While ENSO-related moisture signals extend above 850 hPa (Fig. 5d), most of the ENSO divergence anomalies occur in the lower 1000–850-hPa layer (Fig. 5e), and so does ENSO moisture divergence (Fig. 5f).

Overall, one thus expects 1000–850-hPa divergence anomalies to play a strong role in controlling both the total V_{lf} [Eq. (4.1) of Yu and Neelin 1997] and its interannual anomalies, due to weighting by the large near-surface humidity.

Figure 6 assesses the relation between V_{lf} and the SST-dependent "gross moisture stratification" proposed by Yu and Neelin (1997) and Yu et al. (1998). To that end, we have binned V_{lf} as a function of near-surface (1000–850-hPa average) convergence and SST (Fig. 6a). This figure confirms that V_{lf} is to the first order a linear function of convergence, although some saturation appears for divergent surface circulations (we will come back to this in the discussion section). Given this relationship, V_{lf} can be approximated as

$$V_{lf} \approx V = -m(T)(d - d_0), \qquad (4)$$

with the average 1000–850-hPa divergence denoted as d; $d_0 \approx -0.2$ day^{-1}. The d_0 term needs to be accounted for when using Eq. (4) to recompute the total rainfall but can be neglected when applying this equation to ENSO rainfall anomalies (not shown); we will nonetheless retain it in the rest of the paper. The SST-dependent gross moisture stratification $m(T)$ (with SST denoted as T) can be obtained as the slope of the various curves ion Fig. 6a, and is displayed in red in Fig. 6b. It can be fitted as $m(T) = m_0 e^{\beta(T-T_0)}$ (black curve in Fig. 6b) where $T_0 = 25°C$, $\beta = 0.28°C^{-1}$, and $m_0 = 9$ mm. As detailed in appendix A, one expects m to increase exponentially with SST at a $0.07°C^{-1}$ e-folding rate, due to
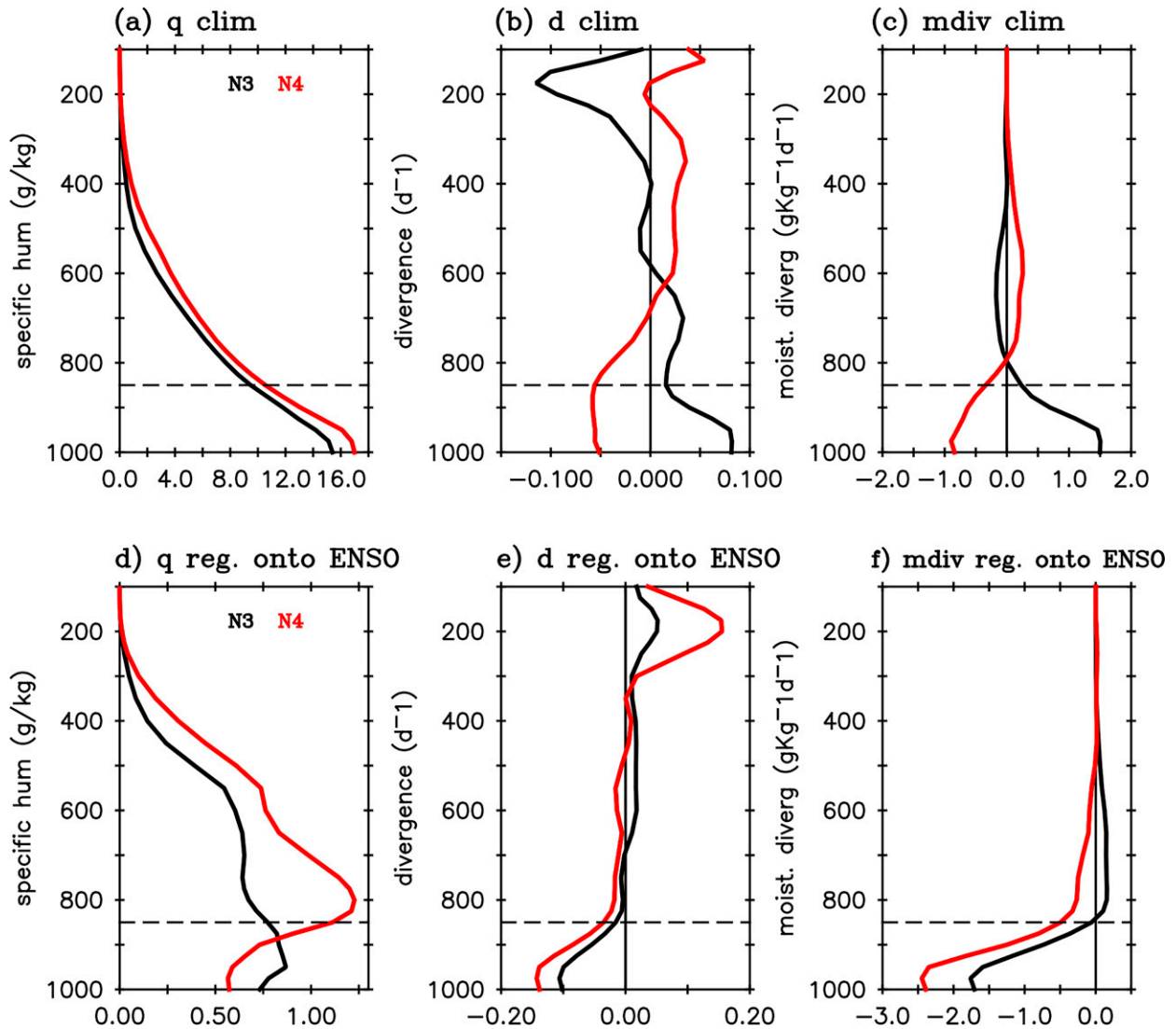
FIG. 5. Vertical profiles of climatological (a) specific humidity (g kg^{-1}), (b) divergence (day^{-1}), and (c) moisture divergence (g kg^{-1} day^{-1}) averaged over Niño-3 (black curve) and Niño-4 (red curve) regions. (d) Specific humidity (g kg^{-1} °C^{-1}), (e) divergence (day^{-1} °C^{-1}), and (f) moisture divergence (g kg^{-1} day^{-1} °C^{-1}) interannual anomalies regressed on normalized Niño-3.4 SST anomalies for both Niño-3 (black curve) and Niño-4 (red curve) regions. The thin dashed line on each panel indicates the upper boundary of what we assume to be the boundary layer (1000–850 hPa).

Clausius–Clapeyron (the saturation humidity increase supported by the underlying high SSTs). The much larger 0.28°C^{-1} e-folding rate of $m(T)$ is related to the SST-dependent vertical atmospheric structure (see appendix A).

By linearizing d and T into their climatological seasonal cycle (overbar) and anomalies ($'$), and recalling that $P' \approx V'_{\text{lf}}$, Eq. (4) leads to the following expression for interannual rainfall anomalies (see appendix B for details):

$$P' \approx P^0(\overline{T}, \overline{d}, T', d')$$
$$= -m(\overline{T})\left[\underbrace{d'}_{\text{DYN}} + \underbrace{\beta(\overline{d} - d_0)T'}_{\text{THD}} + \underbrace{\beta(T'd')'}_{\text{MIX}}\right]. \quad (5)$$

A physical interpretation of the above equation follows. The $-m(\overline{T})$ in front of the equation represents the effect of the background humidity profile $\overline{q}$. It translates the fact that a given divergence anomaly produces a much larger precipitation response at high background SST, due to the combined effect of Clausius–Clapeyron and a thicker moist layer. The first term within the bracket translates the fact that a divergence anomaly d' contributes to rainfall through its influence on the moisture convergence. We will call $-m(\overline{T})d'$ the "dynamical contribution" to rainfall DYN [as, e.g., in Chung et al. (2014)], corresponding to the effect of the anomalous circulation d' on the background humidity profile $\overline{q}$. The second term is often referred to as the "thermodynamical
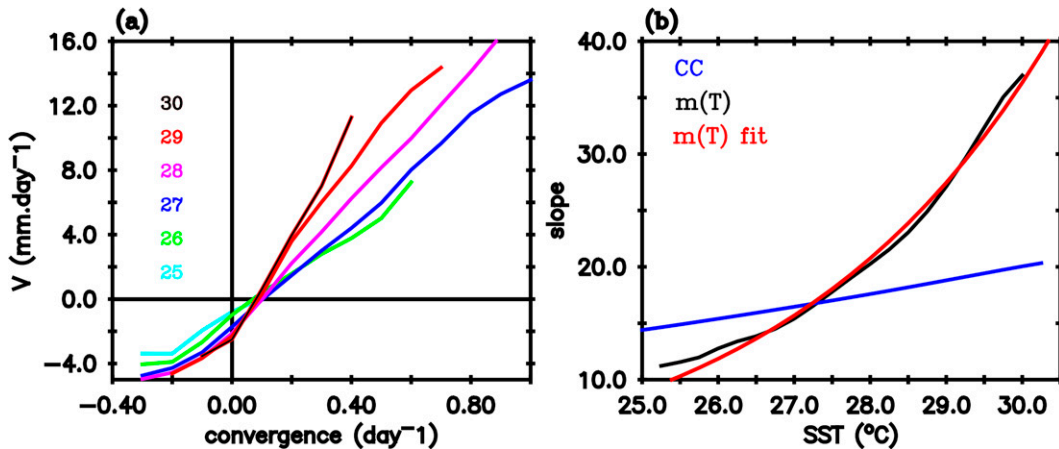
FIG. 6. (a) Low-frequency components of the vertically integrated moisture convergence V_{lf} as a function of 1000–850-hPa average convergence, for various SST. This figure is obtained through binning monthly V_{lf} over the near-equatorial Pacific (120°E–80°W, 10°S–10°N) during the 1979–2019 period into 0.01 day^{-1} convergence and 0.2°C SST bins, and only bins centered on 25°, 26°, 27°, 28°, 29°, and 30°C are displayed as colored curves. (b) Gross moisture stratification $m(T)$ (mm), obtained as the slope of curves in (a) (black curve), its analytical fit (red curve), and increase of rainfall expected from the Clausius–Clapeyron relation at constant relative humidity (blue curve; see text for details).

contribution" to rainfall, THD, corresponding to the effect of the background divergence $\overline{d}$ on the anomalous humidity profile q' [represented by the $-m(\overline{T})\beta T'$ term]. Second-order contributions to this term are negligible and were dropped (see appendix B for details). The $\beta(T'd')'$ term is also second order, but cannot be neglected (see appendix B for details). It is the mixed dynamic–thermodynamical contribution, MIX, corresponding to the effect of the anomalous divergence d' on the anomalous humidity profile q' [represented by the $-m(\overline{T})\beta T'$ term]. As we will see later, this nonlinear term plays an important role in the generation of rainfall asymmetries between El Niño and La Niña events. The nonlinearity in the $T'd'$ term implies that it does not average to zero, and its anomaly is thus written as $(T'd')'$: the $-m(\overline{T})\beta\overline{T'd'}$ term represents the ENSO contribution to climatological rainfall due to nonlinearities. While this contribution is small relative to the two dominant components of the climatological P budget $\overline{V}_{lf}$ and $\overline{E}$ seen in Fig. 2 (not shown) it cannot be neglected in the MIX term: it would otherwise introduce a positive bias in the MIX term skewness, which would be an issue when evaluating the contribution of this term to ENSO rainfall anomalies asymmetries.

Figure 7 assesses the ability of Eq. (5) to reproduce ERA5 precipitation anomalies in Niño-3 and Niño-4. The P^0 formula above matches the observed precipitation interannual anomalies almost perfectly, with a 0.98 (0.96) correlation and 0.37 (0.64) mm day^{-1} rms difference over the Niño-3 (Niño-4) region. The amplitude asymmetries between El Niño and La Niña in Niño-3 and Niño-4, with larger rainfall anomalies during El Niño events, are in particular very well reproduced by our P^0 equation (Fig. 7).

To further test the ability of P^0 to reproduce the ENSO rainfall anomalies and the asymmetries between El Niño and La Niña, Fig. 8 shows the symmetrical and asymmetrical

components of ENSO composite rainfall anomalies from GPCP, ERA5, and our P^0 estimate. Those symmetrical and asymmetrical components are respectively obtained as the half-difference and half-sum of the El Niño (including both moderate and extreme events) and La Niña composites, as defined in section 2. The first thing to note is that the GPCP and ERA5 ENSO rainfall anomalies match quite well, both for the symmetric and asymmetric components. In fact, P^0 can also reproduce the ENSO composite symmetrical rainfall pattern very well (Figs. 8b,c), despite a slight overestimate of the signal in the central Pacific and south of the ITCZ (see appendix B for a discussion of the error sources). The agreement is even more convincing for the ENSO rainfall asymmetrical component (Figs. 8e,f). Equation (5) thus reproduces the symmetrical and asymmetrical ENSO rainfall signal very well. In the following section, we will thus use Eq. (5) to diagnose the various physical contributions to ENSO-related rainfall anomalies P' and their asymmetries between El Niño and La Niña.

5. Mechanisms of the El Niño–La Niña precipitation asymmetries

Eliminating d' from Eq. (5) would yield a formula of P' as a function of T' only. This would require a formula of d' as a function of P' through nonlocal Matsuno–Gill dynamics (e.g., Gill 1980), and as a function of T' through its direct action on the boundary layer horizontal pressure gradients (Lindzen and Nigam 1987). We will discuss this perspective in section 6, but this is beyond the goal of the present article, whose main goal is to identify nonlinearities in the P' dependency on SST anomalies T', so that we can quantify the relative role of these nonlinearities and of asymmetries in the anomalous SST forcing in the overall P' asymmetry. We will thus use a statistical
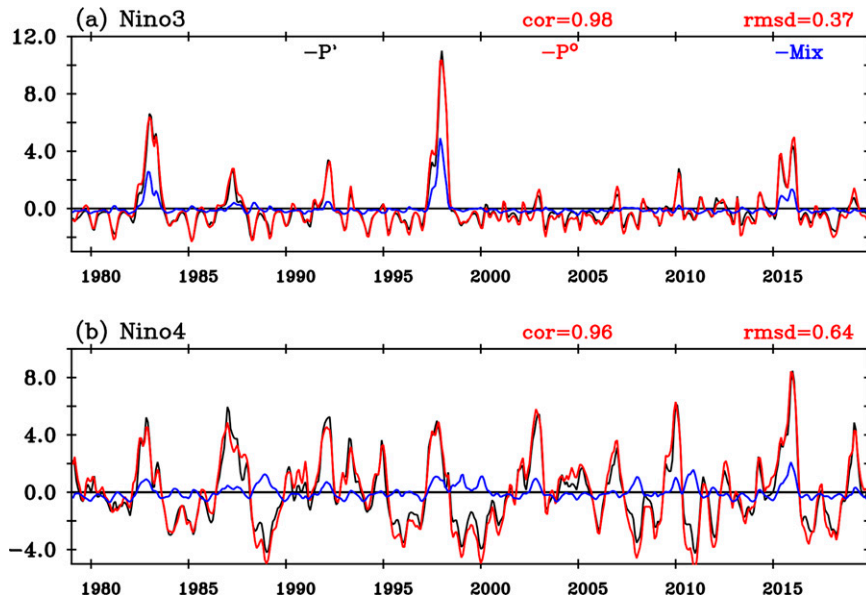
FIG. 7. Time series of average ERA5 precipitation anomalies (P'; black curve; mm day^{-1}) and P^0 [Eq. (5); red curve] analytical relation over the (a) Niño-3 and (b) Niño-4 regions. The blue curve shows the MIX contribution of P^0 from Eq. (7).

approach to split d' into a part that is linearly dependent on SST and a residual that contains nonlinearities. There is indeed an implicit nonlinearity in the dynamical term d'. As demonstrated by the results of Chung et al. (2014) and Chung and Power (2014), the divergence anomaly d' is indeed not a linear response to SST anomalies, in particular due to the convergence feedback (e.g., Zebiak 1986). We thus separate the linear and nonlinear components of the divergence anomalies d' as follows. Previous studies have shown that most of ENSO-related SST variance can be explained from two orthogonal normalized indices of the eastern and central Pacific events E and C (Fig. 9a; Takahashi et al. 2011), deduced from a rotation of the two leading EOFs of the tropical Pacific SST anomalies. Dommenget et al. (2013) showed that these two indices can be used to summarize both the amplitude and pattern asymmetries associated with ENSO SST anomalies. Mayer et al. (2013) further demonstrated that ENSO-related V_{lf} (or equivalently, precipitation or divergence) anomalies could also be summarized using these two uncorrelated indices. We thus obtain the linear part of the divergence response to SST as

$$d'_l = d_E(x, y)E(t) + d_C(x, y)C(t), \qquad (6)$$

where d_E (d_C) is obtained from the regression of d' on the $E(C)$ index (Figs. 9b,c). Figures 9b and 9c show that the divergence anomalies associated with the E pattern are unsurprisingly shifted east relative to those associated with the C pattern, and that both patterns are associated with a dipole corresponding to a meridional shift of the ITCZ. Figure 9e shows the central-western Pacific (red box on Fig. 9c) average d' as a function of the C index, and its linear fit remains systematically within the interquartile distribution (Fig. 9e),

indicating a relatively linear response of divergence around the date line to the C index. Farther east (from the date line to 110°E; see black box in Fig. 9b), the divergence deviates significantly from its linear fit for large positive values of E, highlighting a nonlinear divergence response to SST in the central Pacific for large El Niño events as already discussed by Takahashi and Dewitte (2016). We obtain the nonlinear contribution to the divergence as $d'_{nl} = d' - d'_l$, which allows us to split the dynamical term of Eq. (5) into a linear and a nonlinear contribution (refer to section 6b for a discussion of approximations related to this separation):

$$P^0(\overline{T}, \overline{d}, T', d') \approx -m(\overline{T})\left[\underbrace{d'_l}_{\text{DYN}_l} + \underbrace{d'_{nl}}_{\text{DYN}_{nl}} \right.$$

$$\left. + \underbrace{\beta(\overline{d} - d_0)T'}_{\text{THD}} + \underbrace{\beta(T'd' - \overline{T'd'})}_{\text{MIX}} \right]. \qquad (7)$$

The main contributors to ENSO rainfall anomalies are displayed on Fig. 10, which contrasts composites of P^0 and its four contributors [RHS of Eq. (7)] during the peak phase (December–February average) of El Niño and La Niña events (note that for this analysis the El Niño composite includes both moderate and extreme El Niño events; we will discuss extreme El Niño events separately below). The largest contributor to the overall ENSO rainfall anomaly is the linear component of the dynamical feedback DYN$_l$ (Figs. 10c,i). Positive SST anomalies are indeed generally associated with an enhanced low-level horizontal convergence, yielding stronger rainfall and vice versa. As expected from Eq. (7), the effect of the divergence anomalies is modulated by the background humidity profile $m(\overline{T})$, yielding a much stronger
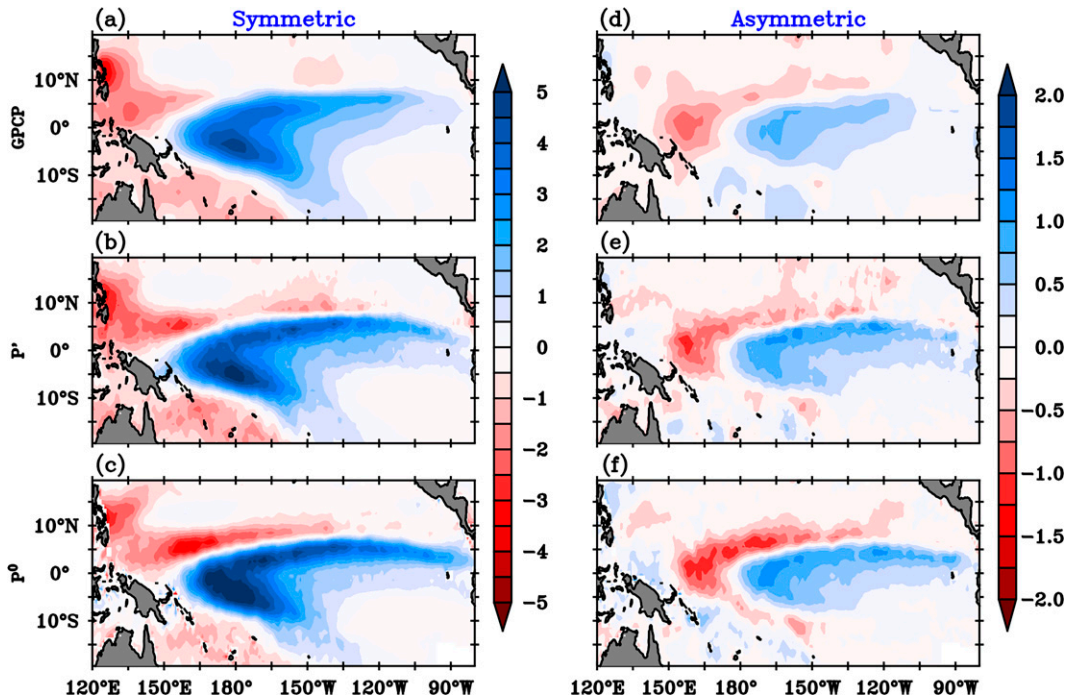
FIG. 8. Average DJF ENSO composite (left) symmetrical [obtained as (Niño − Niña)/2] and (right) asymmetrical [obtained as (Niño + Niña)/2] anomalies for (a),(d) GPCP rainfall, (b),(e) ERA5 rainfall, and (c),(f) P^0 from Eq. (7).

rainfall response at high SST, for instance in the central Pacific (Figs. 10c,i).

Nonlinear contributions to the dynamical feedback (DYN_{nl}) generally tend to strengthen the linear component, especially in the central Pacific where the ENSO rainfall anomalies are largest (Figs. 10d,j). This agrees with Zebiak (1986), who underlined the contribution of the convergence feedback in the central Pacific. The thermodynamical effect also tends to strengthen the dynamical effects (Figs. 10e,k). Warm SST anomalies indeed not only generate anomalous low-level convergence, but also tend to warm and moisten the lower troposphere, leading to enhanced rainfall. This thermodynamical effect is also enhanced in high background SST and convergence regions, due to the $m(\overline{T})$ and $\overline{d} - d_0$ terms in Eq. (6).

While the linear and nonlinear dynamical terms and the thermodynamical term all tend to combine constructively to produce the La Niña and El Niño rainfall patterns, the nonlinear MIX $-m(\overline{T})\beta(T'd')'$ term has a more distinct spatial pattern. Figure 11 allows us to understand how this spatial pattern emerges, by separately showing its $-m(\overline{T})\beta T'd'$ El Niño and La Niña composites, and the constant contribution to this term $-m(\overline{T})\beta\overline{T'd'}$. As explained earlier, this constant contribution is required to ensure that the MIX long term mean is zero: it corresponds to ENSO contribution to the mean state rainfall through atmospheric nonlinearities, of up to 2 mm day^{-1} just east of the date line (Fig. 11c; 12% of the Niño-4 DJF rainfall).

The terms T' and d' are negatively correlated, because anomalous convergence tends to occur over warm anomalies and divergence over cold ones. The $-m(\overline{T})\beta T'd'$ term is thus

almost always positive, during both El Niño and La Niña (Figs. 11a,b). Physically, it can be explained as follows: the positive low-level convergence and specific humidity combine to produce a stronger moisture convergence over warm anomalies. On the other hand, over cold anomalies, the drying effect of the divergence anomaly is made less efficient by the lower humidity loading in the lower troposphere. The ~20° longitude (2000 km) westward shift of T' and d' during La Niña relative to El Niño (Figs. 10a,g) also induces a westward shift of $-m(\overline{T})\beta T'd'$ (Figs. 11a,b). When subtracting the $-m(\overline{T})\beta\overline{T'd'}$ contribution displayed in Fig. 11c, this explains why the MIX term becomes slightly negative in the western Pacific during El Niño events (Fig. 10f) and in the central Pacific during La Niña events (Fig. 10l).

But overall, the main effect of the MIX term is to enhance rainfall in the central and eastern Pacific during El Niño events, east of the maximum positive rainfall anomalies (Fig. 10f). During La Niña events, the MIX term is also positive in the western Pacific, where the dry anomalies tend to be maximum (Fig. 10l). This term thus acts to enhance El Niño wet and reduce La Niña dry rainfall anomalies (Fig. 7). This is therefore an important term contributing to the rainfall amplitude asymmetry between El Niño and La Niña.

Figure 12 displays the composite ENSO symmetrical and asymmetrical components of the Eq. (7) rainfall budget. The symmetrical component confirms that the linear DYN term dominates the budget, that the nonlinear DYN term (DYN_{nl}) enhances the effect of the linear term in the central Pacific, and that the thermodynamical term THD operates mostly
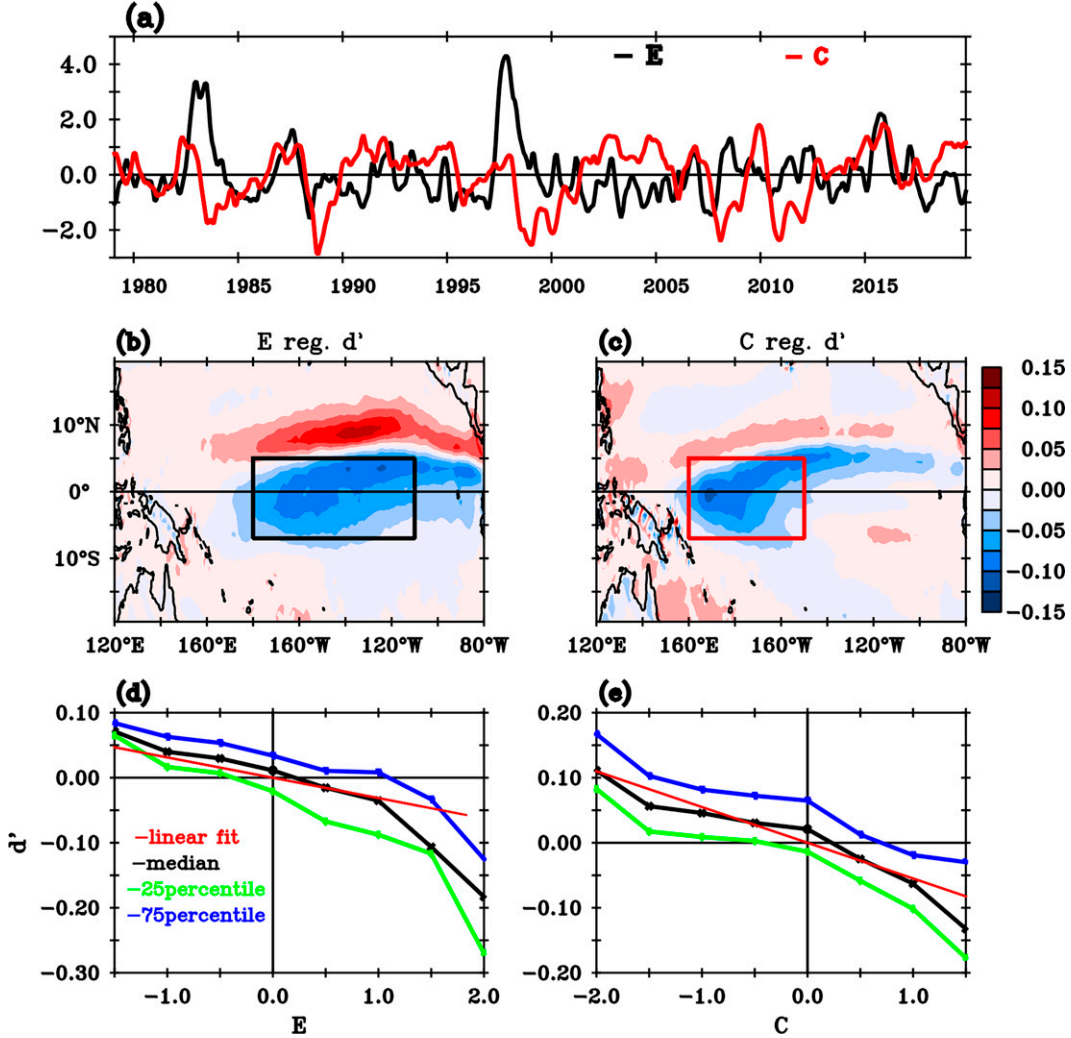
FIG. 9. (a) Time series of E and C ENSO indices computed as in Takahashi et al. (2011). Spatial patterns of surface divergence anomalies regressed onto the (b) E and (c) C indices. (d) Distribution (median in red; lower and upper quartiles in green and blue) of the average central Pacific [black box in (b)] divergence anomalies binned as a function of the E index. (e) As in (d) but for central-western [red box in (c)] divergence anomalies as a function of the C index.

under the ITCZ and SPCZ (Figs. 12b–e). This analysis also indicates that the MIX term is a key source of atmospheric nonlinearity that contributes to El Niño–induced wet anomalies, but offsets La Niña–induced rainfall anomalies in the central Pacific (Fig. 12l). While the MIX term mainly contributes to the central-eastern Pacific skewed ENSO rainfall distribution, the thermodynamical term and both the linear and nonlinear dynamical terms all contribute to the westward La Niña pattern shift (Figs. 12h–k).

As discussed in the introduction, atmospheric nonlinearities and the westward shift of the La Niña SST pattern relative to that of El Niño both contribute to the ENSO asymmetrical rainfall response. Below, we estimate the contribution of each of these factors to the overall ENSO asymmetrical precipitation response. The asymmetrical component of the ENSO rainfall can be approximated (see appendix C for a full

derivation; letter a subscripts indicate the asymmetrical and letter s the symmetrical components) as shown below:

$$P_a^0 = -m(\overline{T}) \left[\underbrace{\beta(\overline{d} - d_0)T_a' + d_{la}'}_{\text{SST forcing}} \right.$$

$$\left. + \underbrace{d_{\text{nl}a}' + \beta\left(d_a'T_a' + d_s'T_s' - \overline{d'T'}\right)}_{\text{Atmospheric nonlinearity}} \right]. \quad (8)$$

The terms d_{la}' and $d_{\text{nl}\,a}'$ designate the linear and nonlinear components of the divergence anomaly response to the SST forcing T_a', obtained through Eq. (6) and its residual. The first two terms in the brackets of the RHS of Eq. (8) linearly depend on T_a': they represent the part of rainfall anomalies that are directly forced by SST asymmetries. The remaining
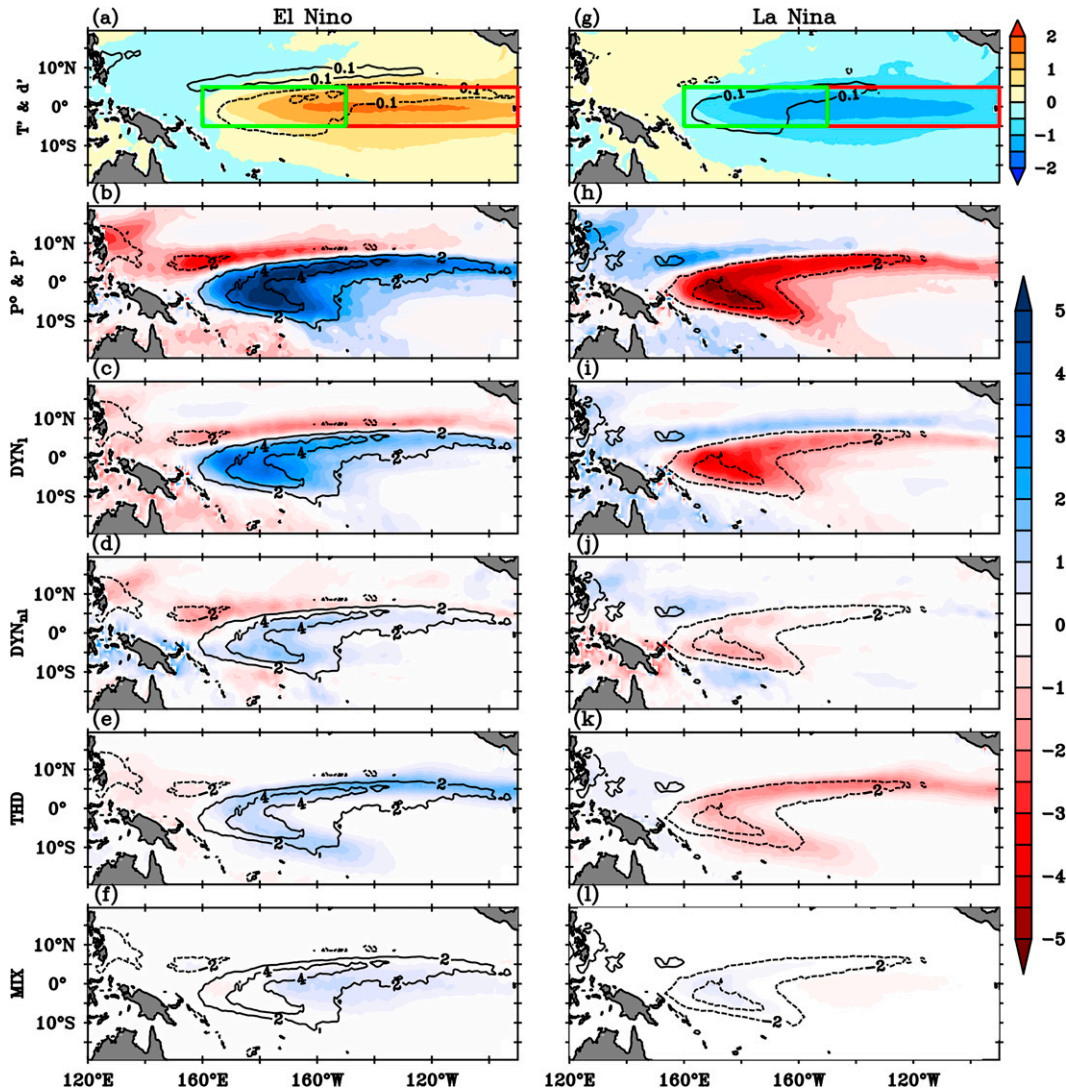
FIG. 10. Average DJF El Niño composite anomalies of (a) SST (T'; shading; °C) and divergence (d'; contours; day^{-1}), (b) P^0 (shading; mm day^{-1}), and of various P^0 budget terms [see Eq. (7)]: (c) linear (DYN$_l$) and (d) nonlinear dynamical (DYN$_{nl}$) terms, (e) thermodynamical (THD) term, and (f) mixed dynamical–thermodynamical (MIX) term. (g)–(l) As in (a)–(f), but for La Niña. The P' composites (mm day^{-1}) for El Niño and La Niña events are respectively displayed as contours in (b)–(f) and (h)–(l). The El Niño composites on this figure include both moderate and extreme El Niño events.

terms in Eq. (8) are nonlinear. These terms include a contribution from asymmetrical signals, for instance the $d'_a T'_a$ contribution from the MIX term. In practice, this contribution is small (not shown), because d'_a and T'_a are much smaller than their symmetrical counterparts (see Figs. 12a,g). We will thus consider that this term mainly represents the effect of atmospheric nonlinearities.

The first two terms of Eq. (8) are thus summed and represent the part of the ENSO rainfall asymmetrical response (Fig. 13a) that is forced by the asymmetrical SST pattern (Fig. 13b), while the last two terms (Fig. 13c) represent the effect of atmospheric nonlinearities. The ENSO rainfall asymmetrical component (Fig. 13a) displays a clear dipole pattern,

with positive anomalies in the central and eastern Pacific and negative anomalies in the western Pacific and under the ITCZ. Positive values in the central Pacific indicate that El Niño wet anomalies are larger than La Niña dry anomalies in this region (also see Figs. 10b,h). Negative values west of the date line correspond to the westward extension of the La Niña dry anomalies related to the El Niño wet anomalies (also see Figs. 10b,h). Table 1 allows us to quantify the atmospheric nonlinearities and SST contributions to the ENSO rainfall asymmetries in the central and eastern (175°E–90°W, 5°N–5°S) and western Pacific (145°–175°E, 5°N–5°S; see boxes in Fig. 13). Our decomposition indicates that the larger-amplitude rainfall anomalies associated with El Niño in the
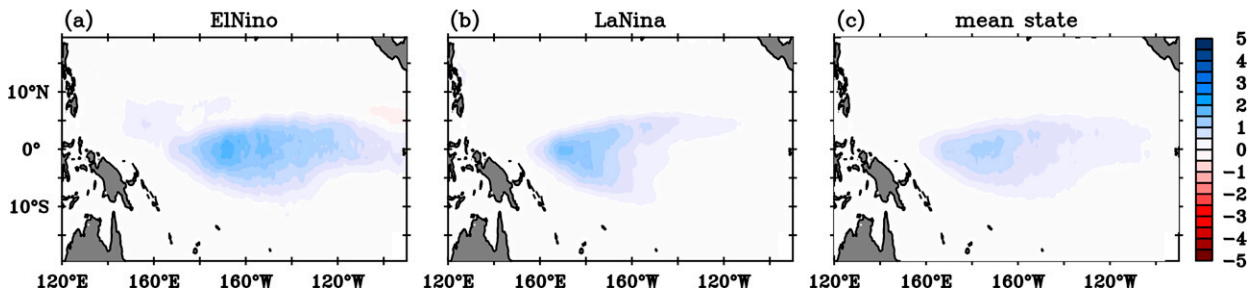
FIG. 11. Average DJF of the (a) El Niño and (b) La Niña composites of the $-m(\overline{T})\beta T'd'$ contribution to the mixed dynamical–thermodynamical (MIX) term. (c) Average DJF of the $-m(\overline{T})\beta\overline{T'd'}$ constant contribution to the MIX term, also corresponding to the ENSO contribution to the DJF climatological rainfall due to the effect of atmospheric nonlinearities.

central and eastern Pacific can mainly be attributed to atmospheric nonlinearities (~70%; Table 1, Figs. 13a,c). On the other hand, the westward extension of La Niña dry anomalies into the western Pacific has ~50% contributions from the SST forcing asymmetry and the internal atmospheric nonlinearities.

In the above analysis, we simply considered the overall asymmetries between El Niño and La Niña but did not specifically discuss extreme El Niño events. Takahashi and Dewitte (2016) suggested that atmospheric convective nonlinearities play a key role in generating intense rainfall anomalies in the equatorial eastern Pacific during these strong El Niño events. Figure 7 confirms that: the MIX term becomes nonnegligible in the Niño-3 region during each of the three extreme El Niño events in the record (1982/83, 1997/98, and 2015/16). Figure 14 provides a composite evolution of the various terms of the atmospheric water budget in Niño-3 during extreme El Niño events based on Eq. (7). We do not show moderate El Niño or La Niña events composites, for which anomalies over the eastern equatorial Pacific are weak. On the other hand, wet anomalies of up to 7 mm day^{-1} occur in the Niño-3 region at the peak of extreme El Niño events (Fig. 14a). The two largest contributors to the El Niño peak rainfall anomalies are the mixed MIX and linear dynamical DYN$_l$ terms. The mixed term accounts for ~40% of the DJF Niño-3 rainfall (Fig. 14a), confirming that internal atmospheric nonlinearities related to the anomalous transport of anomalous moisture play a key role in the generation of the extreme El Niño large eastern Pacific rainfall anomalies. When also considering nonlinearities associated with the dynamical term (blue DYN$_{nl}$ curve, accounting for 13%), nonlinearities associated with the deep atmospheric convection contribute to about 50% of the December–February eastern Pacific rainfall anomaly during extreme El Niño events.

In this section, we have demonstrated that the nonlinear moisture transport plays a key role in the rainfall asymmetry between El Niño and La Niña in the central and eastern Pacific, being a large term in the eastern Pacific anomalous moisture budget during extreme El Niños (~40% of the total rainfall anomaly; Fig. 14a). Overall, atmospheric nonlinearities contribute to about 70% of the larger El Niño than La Niña wet anomalies in the central and eastern Pacific, and to about half of larger La Niña than El Niño dry anomalies in the western Pacific (Fig. 13 and Table 1).

6. Summary and discussion

a. Summary

It is important to understand the asymmetrical rainfall response to ENSO, because it appears to play a strong role in ENSO overall asymmetries, the development of extreme El Niño events (e.g., Kang and Kug 2002; Frauen and Dommenget 2010; Im et al. 2015; Takahashi and Dewitte 2016; Geng et al. 2019) and how the mean state and ENSO respond to anthropogenic climate change (e.g., Power et al. 2013; Karamperidou et al. 2017; Cai et al. 2018). In the present study, we assess the respective contribution of SST asymmetrical forcing and atmospheric nonlinearities on the asymmetrical rainfall response to ENSO based on a vertically integrated water budget applied to the ERA5 reanalysis (Hersbach et al. 2020).

We first show that interannual rainfall anomalies are dominated by interannual variations of the vertically integrated moisture convergence (VIMC), and that subseasonal winds and humidity variations hardly contribute to this term, which can thus be computed from seasonally averaged quantities. Following ideas developed by Neelin and Held (1987) and Yu and Neelin (1997, 1998), we then derive a simplified equation for VIMC, under the form of a SST-dependent "gross moisture stratification" multiplied by the boundary layer (taken as the 850–1000-hPa average) divergence. Gross moisture stratification can be approximated from an exponential of SST, with an e-folding scale of 0.28 K^{-1}. This value is considerably larger than the 0.07 K^{-1} expected from the Clausius–Clapeyron relation, because the vertical structure of divergence and humidity is SST dependent and leads to a larger VIMC for a given surface divergence value at high SST and hence much larger ENSO rainfall anomalies per unit of divergence anomaly at high background SST. The specific nature of this dependence will be analyzed in a subsequent study.

The above relation allows deriving a simple and realistic equation for rainfall interannual anomalies as a function of SST and boundary layer divergence background state and anomalies. Its analysis reveals that climatological moisture transport by the anomalous circulation (i.e., "dynamical" contribution) contributes most to ENSO rainfall anomalies, reinforced by transport of anomalous moisture by the
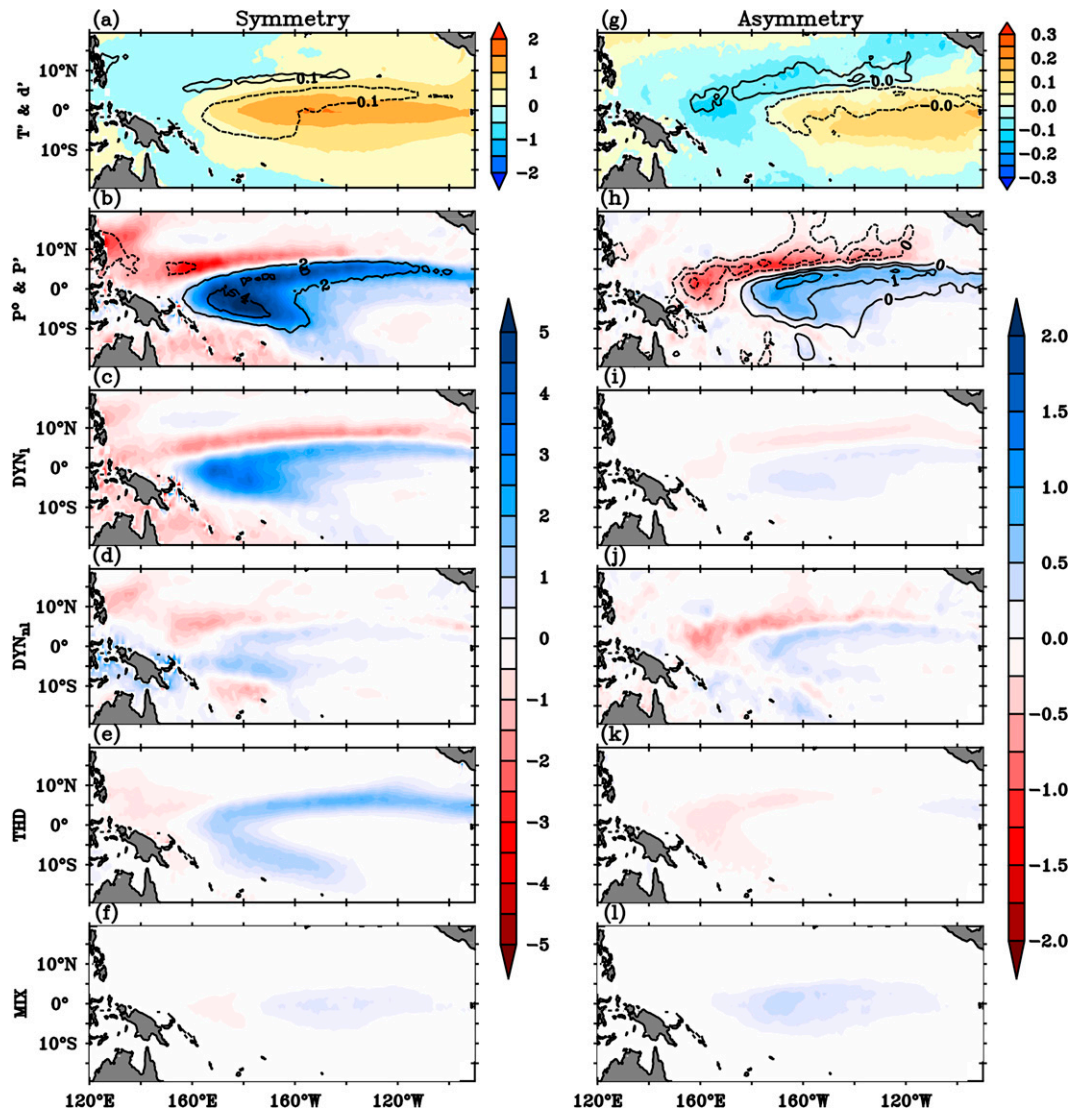
FIG. 12. Average DJF of the ENSO composite (left) symmetrical [obtained from Fig. 10 as (Niño − Niña)/2] and (right) asymmetrical [obtained from Fig. 10 as (Niño + Niña)/2] anomalies. (a),(g) SST (T'; shading; °C) and divergence (d'; contours; day^{-1}), (b),(h) P^0 (shading; mm day^{-1}), and of various P^0 budget terms [see Eq. (7)]: (c),(i) linear (DYN$_l$) and (d),(j) nonlinear dynamical (DYN$_{nl}$) terms, (e),(k) the thermodynamical (THD) term, and (f),(l) the mixed dynamical–thermodynamical (MIX) term.

climatological circulation (the linear "thermodynamical" contribution). A major source of amplitude asymmetry arises from atmospheric nonlinearities, especially the transport of anomalous moisture by the anomalous circulation (i.e., the "mixed" term). Being positive for both El Niño and La Niña, it strengthens El Niño rainfall anomalies and weakens La Niña anomalies. This term in particular contributes to about 40% of the eastern Pacific wet anomalies during the peak of extreme El Niño events. Nonlinearities in the circulation response to SST anomalies also contribute to asymmetries through a nonlinear contribution to the dynamical term. Together, these atmospheric nonlinearities contribute to about 70% of the ENSO positively skewed rainfall anomalies in the central and eastern Pacific

and about 50% of the negatively skewed rainfall anomalies in the western Pacific.

b. Discussion

Most of the assumptions made when deriving the P^0 equation are accurate, as can be testified by the very good agreement between this estimate and the actual rainfall interannual anomalies (Figs. 7, 8). A more questionable assumption, though, is related to the separation of divergence anomalies d' into a linearly and nonlinearly dependent part on SST anomalies, based on the projection on E and C indices [Eq. (6)]. Previous studies (e.g., Takahashi and Dewitte 2016)
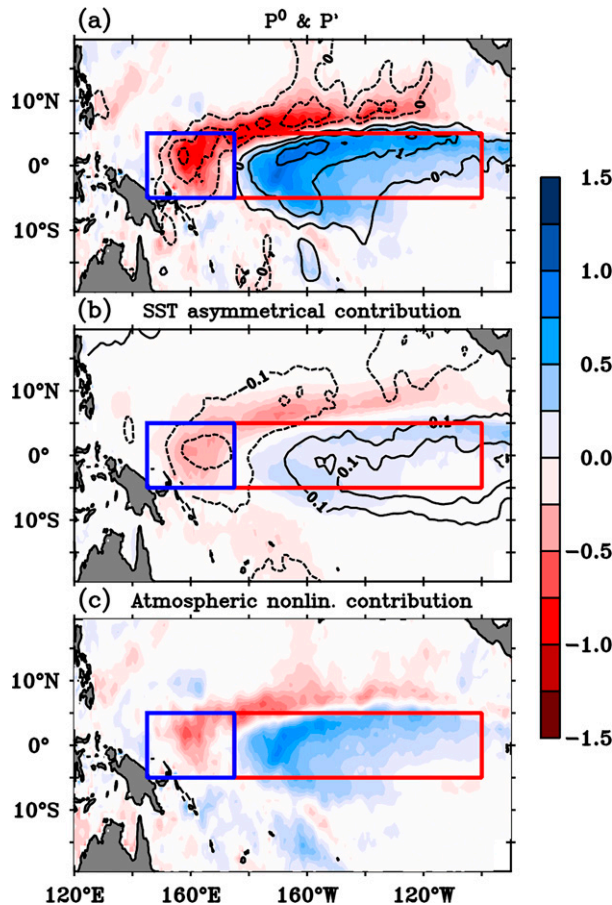
FIG. 13. Average DJF of the ENSO asymmetrical (a) P^0 (shading; mm day^{-1}) and P' (contour; mm day^{-1}) components and its contributions due to (b) the asymmetrical SST forcing (with the contours indicating the SST anomalies) and (c) atmospheric nonlinearities [see Eq. (8)]. The asymmetrical ENSO component is defined as the half sum of El Niño (including both moderate and extreme events) and La Niña composite anomalies. The central-eastern Pacific (CEP; 175°E–90°W, 5°N–5°S) and western Pacific (WP; 145°–175°E, 5°N–5°S) boxes are used to provide the average values in Table 1.

have pointed out that the central-eastern Pacific regime change between the effects from the stable (Lindzen and Nigam 1987) and convective (Gill 1980) mechanisms for generating divergence occurs beyond some positive SST anomaly

TABLE 1. Average P^0 ENSO asymmetrical components in the central eastern Pacific (CEP; 175°E–90°W, 5°N–5°S) and western Pacific (WP; 145°–175°E, 5°N–5°S) boxes (see Fig. 13), and contributions from the SST asymmetrical forcing and atmospheric nonlinearities [cf. Eq. (8)].

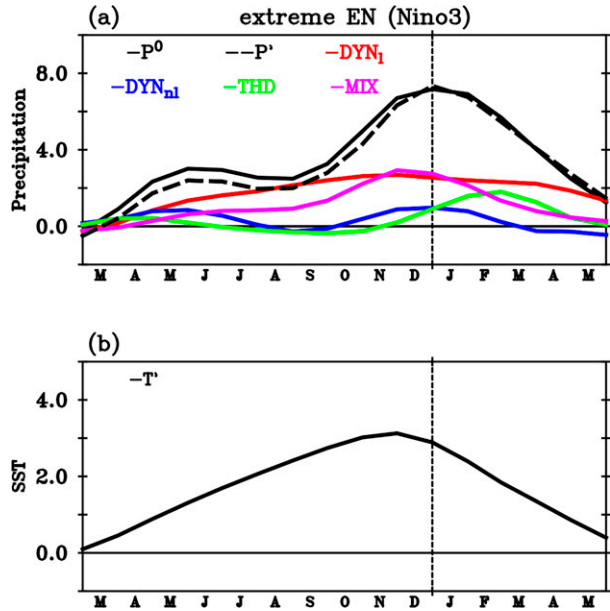|	P^0 asymmetry (mm)	SST contribution (%)	Atmospheric nonlinear contribution (%)
CEP	0.42	30	70
WP	−0.43	53	47

FIG. 14. Extreme El Niño composite life cycle averaged over the Niño-3 region for (a) the ERA5 interannual anomalies P' (black dashed curve), P^0 [from Eq. (7), black curve], and its contributors (mm day^{-1})—linear (DYN$_l$; red) and nonlinear dynamical (DYN$_{nl}$; blue) terms, the thermodynamical (THD; green) term, and the mixed dynamical–thermodynamical (MIX; magenta) term—and (b) SST anomalies.

threshold (corresponding to the $E = 1$ value in Fig. 9d). We should thus in principle have performed separate regressions over the range covered by each regime. From a practical perspective, however, a piecewise linear regression and the linear fit for $E < 1$ are very similar, hence justifying our approximate method for estimating d'_{nl}. In addition, independent results from AGCM sensitivity experiments to be reported in a future study give very similar estimates of the partition of the rainfall asymmetrical response into atmospheric nonlinearities and the SST asymmetrical forcing to those of Fig. 13 based on our analytical approach (not shown). We hence believe that our estimates of the direct role of atmospheric nonlinearities for generating ENSO rainfall asymmetries are reasonably robust.

Let us now discuss our main results against those obtained by previous studies. By examining the tropical water budget in the NCEP reanalysis, Rao et al. (1998) did show that vertically integrated moisture convergence dominates ENSO-related interannual variations, in agreement with our results. Other studies did use a modeling approach to study ENSO rainfall asymmetries. Hoerling et al. (1997) seminal work indicates that El Niño–La Niña rainfall asymmetries can be qualitatively reproduced by forcing an AGCM with an El Niño and La Niña opposite SST patterns, interpreting this as ENSO asymmetrical rainfall response being largely a consequence of the nonlinear atmospheric processes related to the threshold response of convection to SST. Both our study and that of Chung and Power (2015) indicate that differences

between the moderate and strong El Niño SST patterns also contribute to the asymmetrical ENSO rainfall. Our study further points to a ~50% (when accounting for both the MIX and DYN_{nl} terms) effect of atmospheric nonlinearities for the large eastern Pacific rainfall response to extreme El Niño events in agreement with Takahashi and Dewitte (2016).

Chung et al. (2014) and Chung and Power (2014) also investigated the dominant terms and nonlinearities in the ENSO water budget, but through the use of idealized AGCM experiments. In agreement with our results, they found that the "dynamical" term dominates the symmetrical rainfall response. It is difficult to compare our estimate of nonlinearities with theirs, based on forcing an AGCM with a varying-amplitude El Niño or La Niña SST pattern, but their results indicate equivalent contributions of the dynamical and mixed terms to nonlinearities [see Fig. 4 of Chung and Power (2014) and Fig. 5 of Chung et al. (2014)], while we find a stronger role of the mixed term. This suggests that the nonlinearity of the circulation response to the SST forcing, which plays an important role in the dynamical term, is probably quite sensitive to the convective parameterization in the AGCM.

It is difficult to assess which of our results from ERA5 budgets or Chung et al.'s (2014) AGCM experiments is more trustworthy. As we pointed out earlier, ERA5 tends to have too strong rainfall under the ITCZ and SPCZ, relative to GPCP (Nogueira 2020). While this may cast doubt on our water budget, we remark that this rainfall overestimation mostly concerns the mean seasonal cycle, and that the ENSO rainfall interannual variations are very well reproduced by ERA5 (Figs. 3 and 4). In addition, the atmospheric circulation is also constrained by data in ERA5, which may result in a better estimate of the VIMC. But using a data assimilation product for a budget study is not necessarily bulletproof, as data assimilation introduces extra source and sink terms in order to constrain the solution to remain close to observational estimates. This is apparently not the case here, where the residual from the water budget (which includes the assimilation increments) makes very little contribution to the overall moisture balance. Overall, more ENSO water budget studies based on other datasets and models (e.g., the Coupled Model Intercomparison Project database) may be needed to ascertain the dominant nonlinearity in the rainfall response to ENSO.

While we have focused on the role of atmospheric nonlinearities, many studies also point to oceanic nonlinear processes that could also contribute to ENSO asymmetries. The advection of ENSO ocean temperature anomalies by anomalous currents, also referred to as nonlinear dynamic heating, warms central to eastern Pacific SST, through both its vertical (Zebiak and Cane 1987; An and Jin 2004) and horizontal components (Su et al. 2010), hence strengthening El Niño but weakening La Niña events. The advection of heat associated with tropical instability waves (TIWs) can also contribute to ENSO asymmetries (An 2008; Xue et al. 2020). There is currently no clear consensus on which of these oceanic nonlinearities and atmospheric nonlinearities dominate the overall ENSO asymmetry, as the impacts of these asymmetries have generally been studied separately.

Our results indicate a weaker role of SST asymmetries than of atmospheric nonlinearities in ENSO rainfall anomalies. Given the coupled nature of ENSO, it is more relevant to discuss ENSO asymmetries in terms of the respective roles of oceanic and atmospheric processes. Several studies (e.g., Frauen and Dommenget 2010; Geng et al. 2019; Takahashi et al. 2019) indeed argue that the ENSO SST asymmetries are themselves largely be the result of the convective nonlinearity through the air–sea feedback loop. Our estimates of the atmospheric nonlinearities to the ENSO rainfall asymmetries are thus likely a lower bound. In a future study, we will present a diagnostic approach that attempts to quantify the relative effects of the oceanic and atmospheric nonlinearities on the overall ENSO asymmetry.

Neelin and Held (1987) proposed a nonlinear equation for rainfall as a function of SST. This equation was however difficult to use due to the lack of observational constraints on most of the terms, in particular atmospheric stability and heat fluxes through the atmosphere. Our study confirms the main assumptions made in Neelin and Held (1987) and Yu and Neelin (1997), namely that vertically integrated moisture convergence dominates rainfall variability, and that vertically integrated moisture convergence is strongly related to the surface convergence through gross moisture stratification, which strongly increases at high SST. The gross moisture stratification approach can however yield large errors in regions such as the ITCZ or SPCZ (see, e.g., Back and Bretherton 2006). However, when applying this approach to rainfall anomalies rather than to the total rainfall, our work indicates that these errors tend to be cancelled by those associated with the Taylor expansion truncation when deriving Eq. (5) (see appendix B). This explains why the gross moisture stratification approach works so well for interannual anomalies (Fig. 8). A perspective of this work is thus to obtain an easily usable equation for rainfall interannual anomalies as a function of SST anomalies only [i.e., to eliminate the divergence anomalies from Eq. (5)]. The main difficulty is thus to express those divergence anomalies as a function of rainfall anomalies through Matsuno–Gill dynamics (e.g., Gill 1980), and/or as a function of T' through its direct action on the boundary layer horizontal pressure gradients (Lindzen and Nigam 1987). While the study of Neelin and Held (1987) offers some guidance, the functional form of the atmospheric stability, convective heating and radiative cooling dependence on SST still needs to be investigated in order to provide an easily usable equation that can be fitted to observations or models. We will pursue this in the future.

APPENDIX A

Relation between Vertically Integrated Moisture Convergence and Surface Properties

This appendix contains a simplified derivation of the relation between the vertically integrated moisture flux convergence (VIMC, denoted here as V) and surface properties obtained by Neelin and Held (1987) and Yu and Neelin (1997), using the same approximations. The term V can be computed from the vertical integral of the moisture convergence over the atmospheric column as follows:

$$V = \frac{1}{g}\int \nabla(q\mathbf{u})dp. \tag{A1a}$$

While humidity advection clearly cannot be neglected at some pressure levels, we verified that its vertical integral is in general negligible in the tropics. Therefore,

$$V = \frac{1}{g}\int q\nabla\mathbf{u}\,dp. \tag{A1b}$$

We note the 1000–850-hPa average humidity, divergence, and temperature q_s, d_s, and T_s. The Clausius–Clapeyron relation allows computing q_s from T_s and relative humidity r:

$$q_s = rAe^{\gamma T_s}, \tag{A2}$$

with A and γ being 0.003 g kg^{-1} and 0.07 K^{-1} respectively. We verified that $T_s \approx T - \Delta$, where T is the SST and Δ is a climatological air–sea temperature difference. Noting $A' = rAe^{-\gamma\Delta}$, we get

$$q_s = rAe^{-\gamma\Delta}e^{\gamma T} \approx A'e^{\gamma T}. \tag{A3}$$

Let us now assume that the moisture and divergence vertical structures only depend on the SST T (with e.g., thicker atmospheric boundary layer at higher T):

$$d(x,y,p,t) = d_s(x,y,t)d^*(p,T) + d^{\tilde{}}(p,T), \tag{A4a}$$

$$q(x,y,p,t) = q_s(x,y,t)\,q^*(p,T) + q^{\tilde{}}(p,T). \tag{A4b}$$

Combining Eqs. (A1b), (A3), (A4a), and (A4b) leads to

$$V = m(T)d_s, \text{ where } m(T) = A'e^{\gamma T}\frac{1}{g}\int d^*q^*\,dp + \frac{1}{g}\int d^{\tilde{}}q^*\,dp. \tag{A4c}$$

The term $m(T)$ was referred to as "gross moisture stratification" by Yu and Neelin (1997). Yu et al. (1998) found that m strongly depends on SST. The above equation indicates that part of this dependence arises from Clausius–Clapeyron (the $A'e^{\gamma T}$ term), and that part of this dependence is related to the dependency of the divergence and humidity vertical structures on SST (the $\int d^*q^*\,dp$ term). In the present study, we find that this vertical structure dependence on SST boosts the effect of Clausius–Clapeyron, and that m has an exponential dependence on SST, but with a

0.28 K^{-1} e-folding scale, compared to the 0.07 K^{-1} e-folding scale expected from Clausius–Clapeyron, as seen in Fig. 6.

APPENDIX B

Equation for Interannual Precipitation Anomalies

In this appendix, we derive a simplified equation for ENSO rainfall anomalies. In the text of the paper, we show that the vertically integrated moisture convergence anomalies dominate rainfall interannual anomalies:

$$V = -m(T)(d - d_0), \tag{B1}$$

$$m(T) = m_0 e^{\beta(T-T_0)}. \tag{B2}$$

We note interannual anomalies using a prime and the background climatological seasonal cycle with an overbar (e.g., $T = \overline{T} + T'$). For Eq. (B2), we get

$$m(\overline{T} + T') = m_0 e^{\beta T'}e^{\beta(\overline{T}-T_0)} = e^{\beta T'}m(\overline{T}). \tag{B3}$$

Inserting Eq. (B3) into Eq. (B1) and using $d = \overline{d} + d'$, we get

$$V = -m(\overline{T})e^{\beta T'}(\overline{d} - d_0 + d').$$

By doing a Taylor expansion of the $e^{\beta T'}$ to the second order, we get

$$V = -m(\overline{T})[1 + \beta T' + (\beta T')^2/2 + \cdots](\overline{d} - d_0 + d'),$$

$$V = -m(\overline{T})\Big[\overline{d} - d_0 + d' + \beta(\overline{d} - d_0)T' \\ + \beta T'd' + (\overline{d} - d_0)\frac{(\beta T')^2}{2} + \cdots\Big].$$

The second-order term $(\overline{d} - d_0)(\beta T')^2/2$ is negligible relative to the other second-order term $\beta T'd'$ in the tropical Pacific (the ratio of the standard deviation of these two terms is respectively 0.07 and 0.04 in Niño-3 and Niño-4), hence

$$V \approx -m(\overline{T})[\overline{d} - d_0 + d' + \beta(\overline{d} - d_0)T' + \beta T'd'].$$

Taking the climatology, we get

$$\overline{V} = -m(\overline{T})\Big(\overline{d} - d_0 + \beta\overline{T'd'}\Big). \tag{B4}$$

The $\beta\overline{T'd'}$ corresponds to the ENSO contribution to mean state rainfall through atmospheric nonlinearities. While this contribution to the climatological rainfall is relatively small compared to the dominant terms displayed in Fig. 2, it is not negligible relative to interannual anomalies (especially in Niño-4) and needs to be retained when computing $V' = V - \overline{V}$ (it would otherwise introduce an erroneous positive skew in the V' estimate).
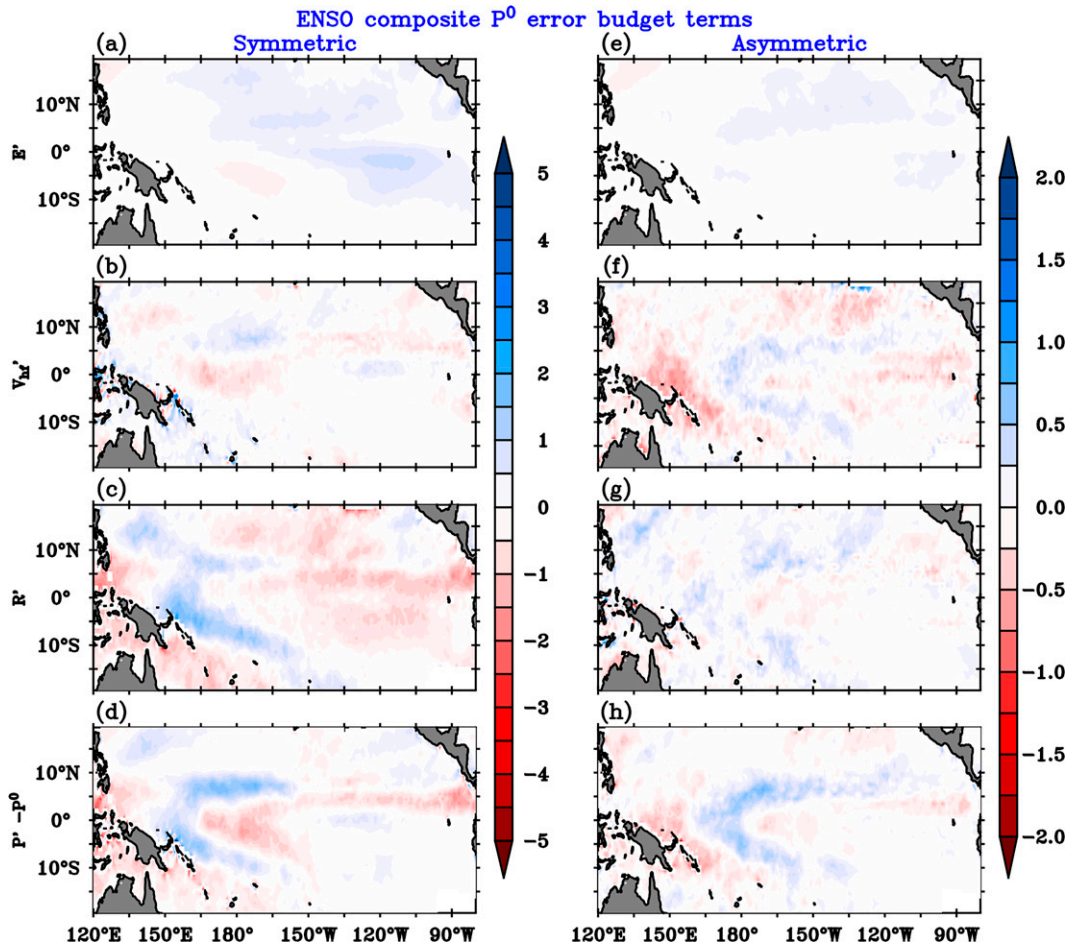
FIG. B1. Average DJF ENSO (left) symmetrical (obtained as the half difference of the El Niño and La Niña composites) and (right) asymmetrical (obtained as the half sum of the El Niño and La Niña composites) of (a),(e) the ERA5 evaporation anomalies E', (b),(f) the intraseasonal variability contribution to the vertically integrated moisture convergence V'_{hf}, (c),(g) the residual R', and (d),(h) $P' - P^0$ [see Eq. (B6) of appendix B and the related text for a discussion of the P^0 error budget].

Recalling that $P' \approx V'$, this gives the equation for our interannual rainfall anomalies estimate P^0:

$$P^0 = -m(\overline{T})\left[d' + \beta(\overline{d} - d_0)T' + \beta(T'd' - \overline{T'd'})\right]. \quad \text{(B5)}$$

The main text of the paper details the physical meaning of the above terms. Below, we provide an equation for the source of errors in P^0 and discuss the impact of those errors on the ENSO budget. Combining Eqs. (3) and (4), it is easy to get

$$P' = P^0 + E' + V'_{hf} + R'. \quad \text{(B6)}$$

Sources of errors in P^0 hence include the interannual anomalies of the evaporation E', high-frequency variability contribution to the vertically integrated moisture convergence V'_{hf}, and a residual R' that includes both approximations related to the gross moisture convergence approximation [Eq. (4)] and to dropping high-order terms in the Taylor expansion above. Fortunately, these two errors tend to cancel each other and to diminish the residual R' (not shown).

Figure B1 shows the December–February composite of Eq. (6) for the ENSO symmetrical and asymmetrical components (obtained as the half difference and half sum of the El Niño and La Niña composites, respectively). This figure indicates that the P^0 errors are quite small, for both the ENSO symmetrical and asymmetrical rainfall anomalies components (Figs. B1d,h and 8b,c,e,f). The main source of error for the ENSO symmetrical component is R' (Figs. B1c,d). For the ENSO asymmetrical component, R' and V'_{hf} both contribute to the P^0 error (Figs. B1f,h). But overall, the P^0 errors seem sufficiently small to use P^0 to understand the ENSO rainfall physical causes, and their asymmetries between El Niño and La Niña. Again, we point here that the very good performance of P^0 for ENSO rainfall anomalies come from the fact that errors associated with the gross moisture stratification approach and errors associated with dropping the third and higher-order terms in the Taylor expansion tend to compensate. The former indeed tend to overestimate rainfall anomalies (Fig. 6) while the latter tend to underestimate them

(approximating $e^{\beta T'}$ by $1 + \beta T$). Our approach hence works quite well for interannual rainfall anomalies, but a theory for the total rainfall would need to also account for nonlinearities in the Fig. 6a (i.e., going beyond the gross moisture stratification approach).

APPENDIX C

Equation for the Asymmetrical Component of ENSO Rainfall Anomalies

In this appendix, we derive an equation for the asymmetrical component of ENSO rainfall anomalies as a function of the symmetrical and asymmetrical components of the sea surface temperature and low-level divergence anomalies. For any variable (here the SST anomalies T'), we note the El Niño composite T'_E and the La Niña composite T'_L. The symmetrical and asymmetrical parts of the SST signal can thus be obtained as $T'_s = (T'_E - T'_L)/2$ and $T'_a = (T'_E + T'_L)/2$. Injecting $T'_E = T'_s + T'_a$, $T'_L = T'_s - T'_a$ and similar expressions for divergence anomalies into Eq. (4) yields the following expressions for the El Niño and La Niña rainfall anomalies:

$$P^0\left(\overline{T}, \overline{d}, T'_E, d'_E\right)$$
$$= -m(\overline{T})\left\{ \begin{array}{l} d'_a + \beta\left[(\overline{d} - d_0)T'_a + d'_a T'_a + d'_s T'_a + d'_a T'_s\right] \\ + d'_s + \beta\left[(\overline{d} - d_0)T'_s + d'_s T'_s\right] - \beta\overline{d'T'} \end{array} \right\},$$

$$P^0\left(\overline{T}, \overline{d}, T'_L, d'_L\right)$$
$$= -m(\overline{T})\left\{ \begin{array}{l} d'_a + \beta\left[(\overline{d} - d_0)T'_a + d'_a T'_a - d'_s T'_a - d'_a T'_s\right] \\ - d'_s + \beta\left[-(\overline{d} - d_0)T'_s + d'_s T'_s\right] - \beta\overline{d'T'} \end{array} \right\}.$$

The asymmetrical component of the ENSO rainfall anomaly P'_a is then obtained as

$$P^0_a = (1/2)\left[P^0\left(\overline{T}, \overline{d}, T'_E, d'_E\right) + P^0\left(\overline{T}, \overline{d}, T'_L, d'_L\right)\right],$$

$$P^0_a = -m(\overline{T})\left[d'_a + \beta(\overline{d} - d_0)T'_a + \beta\left(d'_a T'_a + d'_s T'_s - \overline{d'T'}\right)\right].$$

The d'_a term can then be broken into a part that linearly depends on SST anomalies and a nonlinear part, using Eq. (6) in the manuscript.

REFERENCES

Adler, R., and Coauthors, 2018: The Global Precipitation Climatology Project (GPCP) monthly analysis (new version 2.3) and a review of 2017 global precipitation. *Atmosphere*, **9**, 138, https://doi.org/10.3390/atmos9040138.

An, S.-I., 2008: Interannual variations of the tropical ocean instability wave and ENSO. *J. Climate*, **21**, 3680–3686, https://doi.org/10.1175/2008JCLI1701.1.

——, and F.-F. Jin, 2004: Nonlinearity and asymmetry of ENSO. *J. Climate*, **17**, 2399–2412, https://doi.org/10.1175/1520-0442(2004)017<2399:NAAOE>2.0.CO;2.

——, E. Tziperman, Y. Okumura, and T. Li, 2020: ENSO irregularity and asymmetry. *El Niño Southern Oscillation in a Changing Climate, Geophys. Monogr.*, Vol. 253, 153–172.

Back, L. E., and C. S. Bretherton, 2006: Geographic variability in the export of moist static energy and vertical motion profiles in the tropical Pacific. *Geophys. Res. Lett.*, **33**, L17810, https://doi.org/10.1029/2006GL026672.

Bellenger, H., E. Guilyardi, J. Leloup, M. Lengaigne, and J. Vialard, 2014: ENSO representation in climate models: From CMIP3 to CMIP5. *Climate Dyn.*, **42**, 1999–2018, https://doi.org/10.1007/s00382-013-1783-z.

Burgers, G., and D. B. Stephenson, 1999: The "normality" of El Niño. *Geophys. Res. Lett.*, **26**, 1027–1030, https://doi.org/10.1029/1999GL900161.

Cai, W., and Coauthors, 2014: Increasing frequency of extreme El Niño events due to greenhouse warming. *Nat. Climate Change*, **4**, 111–116, https://doi.org/10.1038/nclimate2100.

——, and Coauthors, 2018: Increased variability of eastern Pacific El Niño under greenhouse warming. *Nature*, **564**, 201–206, https://doi.org/10.1038/s41586-018-0776-9.

Capotondi, A., A. T. Wittenberg, J. S. Kug, K. Takahashi, and M. J McPhaden, 2020: ENSO diversity. *El Niño Southern Oscillation in a Changing Climate, Geophys. Monogr.*, Vol. 253, Amer. Geophys. Union, 65–86.

Choi, K. Y., G. A. Vecchi, and A. T. Wittenberg, 2013: ENSO transition, duration, and amplitude asymmetries: Role of the nonlinear wind stress coupling in a conceptual model. *J. Climate*, **26**, 9462–9476, https://doi.org/10.1175/JCLI-D-13-00045.1.

Chung, C. T. Y., and S. B. Power, 2014: Precipitation response to La Niña and global warming in the Indo-Pacific. *Climate Dyn.*, **43**, 3293–3307, https://doi.org/10.1007/s00382-014-2105-9.

——, and ——, 2015: Modelled rainfall response to strong El Niño sea surface temperature anomalies in the tropical Pacific. *J. Climate*, **28**, 3133–3151, https://doi.org/10.1175/JCLI-D-14-00610.1.

——, ——, J. M. Arblaster, H. A. Rashid, and G. L. Roff, 2014: Nonlinear precipitation response to El Niño and global warming in the Indo-Pacific. *Climate Dyn.*, **42**, 1837–1856, https://doi.org/10.1007/s00382-013-1892-8.

Dee, D. P., and Coauthors, 2011: The ERA-Interim reanalysis: Configuration and performance of the data assimilation system. *Quart. J. Roy. Meteor. Soc.*, **137**, 553–597, https://doi.org/10.1002/qj.828.

Deser, C., and J. M. Wallace, 1987: El Niño events and their relation to the Southern Oscillation: 1925–1986. *J. Geophys. Res.*, **92**, 14 189–14 196, https://doi.org/10.1029/JC092iC13p14189.

DeWeaver, E., and S. Nigam, 2002: Linearity in ENSO's atmospheric response. *J. Climate*, **15**, 2446–2461, https://doi.org/10.1175/1520-0442(2002)015<2446:LIESAR>2.0.CO;2.

Dommenget, D., T. Bayr, and C. Frauen, 2013: Analysis of the non-linearity in the pattern and time evolution of El Niño southern oscillation. *Climate Dyn.*, **40**, 2825–2847, https://doi.org/10.1007/s00382-012-1475-0.

Eisenman, I., L. S. Yu, and E. Tziperman, 2005: Westerly wind bursts: ENSO's tail rather than the dog? *J. Climate*, **18**, 5224–5238, https://doi.org/10.1175/JCLI3588.1.

Frauen, C., and D. Dommenget, 2010: El Niño and la Niña amplitude asymmetry caused by atmospheric feedbacks. *Geophys. Res. Lett.*, **37**, L18801, https://doi.org/10.1029/2010GL044444.

Gadgil, S., P. V. Joseph, and N. V. Joshi, 1984: Ocean–atmosphere coupling over monsoon regions. *Nature*, **312**, 141–143, https://doi.org/10.1038/312141a0.

Geng, T., W. Cai, L. Wu, and Y. Yang, 2019: Atmospheric convection dominates genesis of ENSO asymmetry. *Geophys. Res. Lett.*, **46**, 8387–8396, https://doi.org/10.1029/2019GL083213.

——, W. Cai, and L. Wu, 2020: Two types of ENSO varying in tandem facilitated by nonlinear atmospheric convection. *Geophys. Res. Lett.*, **47**, e2020GL088784, https://doi.org/10.1029/2020GL088784.

Gill, A. E., 1980: Some simple solutions for heat-induced tropical circulation. *Quart. J. Roy. Meteor. Soc.*, **106**, 447–462, https://doi.org/10.1002/qj.49710644905.

Graham, N. E., and T. P. Barnett, 1987: Surface temperature, surface wind divergence, and convection over tropical oceans. *Science*, **238**, 657–659, https://doi.org/10.1126/science.238.4827.657.

Ham, Y.-G., and J.-S. Kug, 2012: How well do current climate models simulate two types of El Niño? *Climate Dyn.*, **39**, 383–398, https://doi.org/10.1007/s00382-011-1157-3.

Hersbach, H., and Coauthors, 2020: The ERA5 global reanalysis. *Quart. J. Roy. Meteor. Soc.*, **146**, 1999–2049, https://doi.org/10.1002/qj.3803.

Hoerling, M. P., A. Kumar, and M. Zhong, 1997: El Niño, La Niña, and the nonlinearity of their teleconnections. *J. Climate*, **10**, 1769–1786, https://doi.org/10.1175/1520-0442(1997)010<1769:ENOLNA>2.0.CO;2.

——, J. W. Hurrell, and T. Xu, 2001: Tropical origins for recent North Atlantic climate change. *Science*, **292**, 90–92, https://doi.org/10.1126/science.1058582.

Hoffman, R. N., and S. M. Leidner, 2005: An introduction to the near-real-time QuikSCAT data. *Wea. Forecasting*, **20**, 476–493, https://doi.org/10.1175/WAF841.1.

Holbrook, N. J., and Coauthors, 2020: ENSO-driven ocean extremes and their ecosystem impacts. *El Niño Southern Oscillation in a Changing Climate. Geophys. Monogr.*, Vol. 253, Amer. Geophys. Union, 409–428.

Huaman, L., and C. Schumacher, 2018: Assessing the vertical latent heating structure of the east Pacific ITCZ using the CloudSat CPR and TRMM PR. *J. Climate*, **31**, 2563–2577, https://doi.org/10.1175/JCLI-D-17-0590.1.

Im, S.-H., S.-I. An, S. T. Kim, and F.-F. Jin, 2015: Feedback processes responsible for El Niño–La Niña amplitude asymmetry. *Geophys. Res. Lett.*, **42**, 5556–5563, https://doi.org/10.1002/2015GL064853.

Jin, F.-F., L. Lin, A. Timmermann, and J. Zhao, 2007: Ensemble-mean dynamics of the ENSO recharge oscillator under state-dependent stochastic forcing. *Geophys. Res. Lett.*, **34**, L03807, https://doi.org/10.1029/2006GL027372.

Kang, I.-S., and J.-S. Kug, 2002: El Niño and La Niña sea surface temperature anomalies: Asymmetry characteristics associated with their wind stress anomalies. *J. Geophys. Res.*, **107**, 4372, https://doi.org/10.1029/2001JD000393.

Karamperidou, C., F.-F. Jin, and J. L. Conroy, 2017: The importance of ENSO nonlinearities in tropical Pacific response to external forcing. *Climate Dyn.*, **49**, 2695–2704, https://doi.org/10.1007/s00382-016-3475-y.

Kug, J.-S., F.-F. Jin, and S.-I. An, 2009: Two types of El Niño events: Cold tongue El Niño and warm pool El Niño. *J. Climate*, **22**, 1499–1515, https://doi.org/10.1175/2008JCLI2624.1.

Larkin, N. K., and D. E. Harrison, 2002: ENSO warm (El Niño) and cold (La Niña) event life cycles: Ocean surface anomaly patterns, their symmetries, asymmetries, and implications. *J. Climate*, **15**, 1118–1140, https://doi.org/10.1175/1520-0442(2002)015<1118:EWENOA>2.0.CO;2.

Larson, S. M., and B. P. Kirtman, 2017: Linking preconditioning to extreme ENSO events and reduced ensemble spread. *Climate Dyn.*, **52**, 7417–7433, https://doi.org/10.1007/s00382-017-3791-x.

Lehodey, P., and Coauthors, 2020: ENSO impact on marine fisheries and ecosystems. *El Niño Southern Oscillation in a Changing Climate. Geophys. Monogr.*, Vol. 253, Amer. Geophys. Union, 429–451.

Lengaigne, M., J. P. Boulanger, C. Menkes, G. Madec, P. Delecluse, E. Guilyardi, and J. Slingo, 2004: The March 1997 westerly wind event and the onset of the 1997/98 El Niño: Understanding the role of the atmospheric response. *J. Climate*, **16**, 3330–3343, https://doi.org/10.1175/1520-0442(2003)016<3330:TMWWEA>2.0.CO;2.

——, ——, ——, P. Delecluse, and J. Slingo, 2005: Westerly wind events in the tropical Pacific and their influence on the coupled ocean–atmosphere system. *Earth Climate: The Ocean–Atmosphere Interaction, Geophys. Monogr.*, Vol. 147, Amer. Geophys. Union, 49–69.

Levine, A. F. Z., and F. F. Jin, 2010: Noise-induced instability in the ENSO recharge oscillator. *J. Atmos. Sci.*, **67**, 529–542, https://doi.org/10.1175/2009JAS3213.1.

Lindzen, R. S., and S. Nigam, 1987: On the role of sea surface temperature gradients in forcing low-level winds and convergence in the tropics. *J. Atmos. Sci.*, **44**, 2418–2436, https://doi.org/10.1175/1520-0469(1987)044<2418:OTROSS>2.0.CO;2.

Lloyd, J., E. Guilyardi, and H. Weller, 2012: The role of atmosphere feedbacks during ENSO in the CMIP3 models. Part III: The shortwave feedback. *J. Climate*, **25**, 4275–4293, https://doi.org/10.1175/JCLI-D-11-00178.1.

Mayer, M., K. E. Trenberth, L. Haimberger, and J. T. Fasullo, 2013: The response of tropical atmospheric energy budgets to ENSO. *J. Climate*, **26**, 4710–4724, https://doi.org/10.1175/JCLI-D-12-00681.1.

Neelin, J. D., and I. M. Held, 1987: Modeling tropical convergence based on the moist static energy budget. *Mon. Wea. Rev.*, **115**, 3–12, https://doi.org/10.1175/1520-0493(1987)115<0003:MTCBOT>2.0.CO;2.

Nogueira, M., 2020: Inter-comparison of ERA-5, ERA-Interim and GPCP rainfall over the last 40 years: Process-based analysis of systematic and random differences. *J. Hydrol.*, **583**, 124632, https://doi.org/10.1016/j.jhydrol.2020.124632.

Ohba, M., and H. Ueda, 2009: Role of nonlinear atmospheric response to SST on the asymmetric transition process of ENSO. *J. Climate*, **22**, 177–192, https://doi.org/10.1175/2008JCLI2334.1.

Okumura, Y. M., and C. Deser, 2010: Asymmetry in the duration of El Niño and La Niña. *J. Climate*, **23**, 5826–5843, https://doi.org/10.1175/2010JCLI3592.1.

Olsen, E. T., and Coauthors, 2017: AIRS/AMSU/HSB version 6 data release user guide. Goddard Space Flight Center, NASA, Jet Propulsion Laboratory, California Institute of Technology, 67 pp.

Planton, Y., J. Vialard, E. Guilyardi, M. Lengaigne, and T. Izumo, 2018: Western Pacific oceanic heat content: Better predictor of La Niña than of El Niño. *Geophys. Res. Lett.*, **45**, 9824–9833, https://doi.org/10.1029/2018GL079341.

——, ——, ——, —— and M. McPhaden, 2022: The asymmetric influence of ocean heat content on ENSO predictability in the CNRM-CM5 coupled general circulation model. *J. Climate*, https://doi.org/10.1175/JCLI-D-20-0633.1, in press.

Power, S., F. Delage, C. Chung, G. Kociuba, and K. Keay, 2013: Robust twenty-first-century projections of El Niño and

related precipitation variability. *Nature*, **502**, 541–545, https://doi.org/10.1038/nature12580.

Puy, M., J. Vialard, M. Lengaigne, and E. Guilyardi, 2016: Modulation of equatorial Pacific westerly/easterly wind events by the Madden–Julian oscillation and convectively-coupled Rossby waves. *Climate Dyn.*, **46**, 2155–2178, https://doi.org/10.1007/s00382-015-2695-x.

——, and Coauthors, 2017: Influence of westerly wind events stochasticity on El Niño amplitude: The case of 2014 vs. 2015. *Climate Dyn.*, **52**, 7435–7454, https://doi.org/10.1007/s00382-017-3938-9.

Rao, V. B., S. R. Chapa, and I. F. A. Cavalcanti, 1998: Moisture budget in the tropics and the Walker circulation. *J. Geophys. Res.*, **103**, 13 713–13 728, https://doi.org/10.1029/98JD00943.

Santoso, A., M. J. Mcphaden, and W. Cai, 2017: The defining characteristics of ENSO extremes and the strong 2015/2016 El Niño. *Rev. Geophys.*, **55**, 1079–1129, https://doi.org/10.1002/2017RG000560.

Su, J., R. Zhang, T. Li, X. Rong, J.-S. Kug, and C.-C. Hong, 2010: Causes of the El Niño and La Niña amplitude asymmetry in the equatorial eastern Pacific. *J. Climate*, **23**, 605–617, https://doi.org/10.1175/2009JCLI2894.1.

Takahashi, K., and B. Dewitte, 2016: Strong and moderate nonlinear El Niño regimes. *Climate Dyn.*, **46**, 1627–1645, https://doi.org/10.1007/s00382-015-2665-3.

——, A. Montecinos, K. Goubanova, and B. Dewitte, 2011: ENSO regimes: Reinterpreting the canonical and Modoki El Niño. *Geophys. Res. Lett.*, **38**, L10704, https://doi.org/10.1029/2011GL047364.

——, C. Karamperidou, and B. Dewitte, 2019: A theoretical model of strong and moderate El Niño regimes. *Climate Dyn.*, **52**, 7477–7493, https://doi.org/10.1007/s00382-018-4100-z.

Taschetto, A. S., C. C. Ummenhofer, M. F. Stuecker, D. Dommenget, K. Ashok, R. R. Rodrigues, and S. W. Yeh, 2020: ENSO atmospheric teleconnections. *El Niño Southern Oscillation in a Changing Climate. Geophys. Monogr.*, Vol. 253, Amer. Geophys. Union, 309–335.

Timmermann, A., and Coauthors, 2018: El Niño–Southern Oscillation complexity. *Nature*, **559**, 535–545, https://doi.org/10.1038/s41586-018-0252-6.

Trenberth, K., and Coauthors, Eds., 2020: The climate data guide: Niño SST indices (Niño 1 + 2, 3, 3.4, 4; ONI and TNI). Last modified 21 January 2020, https://climatedataguide.ucar.edu/climate-data/nino-sst-indices-nino-12-3-34-4-oni-and-tni.

Xue, A., F.-F. Jin, W. Zhang, J. Boucharel, S. Zhao, and X. Yuan, 2020: Delineating the seasonally modulated nonlinear feedback onto ENSO from tropical instability waves. *Geophys. Res. Lett.*, **47**, e2019GL085863, https://doi.org/10.1029/2019GL085863.

Yu, J.-Y., and J. D. Neelin, 1997: Analytic approximations for moist convectively adjusted regions. *J. Atmos. Sci.*, **54**, 1054–1063, https://doi.org/10.1175/1520-0469(1997)054<1054:AAFMCA>2.0.CO;2.

——, C. Chou, and J. D. Neelin, 1998: Estimating the gross moist stability of the tropical atmosphere. *J. Atmos. Sci.*, **55**, 1354–1372, https://doi.org/10.1175/1520-0469(1998)055<1354:ETGMSO>2.0.CO;2.

Zebiak, S. E., 1986: Atmospheric convergence feedback in a simple model for El Niño. *Mon. Wea. Rev.*, **114**, 1263–1271, https://doi.org/10.1175/1520-0493(1986)114<1263:ACFIAS>2.0.CO;2.

——, and M. A. Cane, 1987: A model El Niño–Southern Oscillation. *Mon. Wea. Rev.*, **115**, 2262–2278, https://doi.org/10.1175/1520-0493(1987)115<2262:AMENO>2.0.CO;2.